Geochemistry Geophysics Geosystems G3
AN ELECTRONIC JOURNAL OF THE EARTH SCIENCES
Published by AGU and the Geochemical Society

Article
Volume 9, Number 5
15 May 2008
Q05004, doi:10.1029/2008GC001959
ISSN: 1525-2027

MORB generation beneath the ultraslow spreading Southwest Indian Ridge (9–25°E): Major element chemistry and the importance of process versus source

Jared J. Standish
Geology and Geophysics, Woods Hole Oceanographic Institution, Woods Hole, Massachusetts 02543, USA

Now at Earth and Planetary Sciences, Harvard University, Cambridge, Massachusetts 02138, USA (standish@fas.harvard.edu)

Henry J. B. Dick
Geology and Geophysics, Woods Hole Oceanographic Institution, Woods Hole, Massachusetts 02543, USA

Peter J. Michael
Department of Geosciences, University of Tulsa, Tulsa, Oklahoma 74104, USA

William G. Melson and Timothy O'Hearn
Department of Mineral Sciences, U.S. National Museum of Natural History, Washington, D. C. 20013, USA

[1] We report highly variable mid-ocean ridge basalt (MORB) major element and water concentrations from a single 1050-km first-order spreading segment on the ultraslow spreading Southwest Indian Ridge, consisting of two supersegments with strikingly different spreading geometry and ridge morphology. To the east, the 630 km long orthogonal supersegment (<10° obliquity) dominantly erupts normal MORB with progressive K/Ti enrichment from east to west. To the west is the 400 km long oblique supersegment (up to 56° obliquity) with two robust volcanic centers erupting enriched MORB and three intervening amagmatic accretionary segments erupting both N-MORB and E-MORB. The systematic nature of the orthogonal supersegments' ridge morphology and MORB composition ends at 16°E, where ridge physiography, lithologic abundance, crustal structure, and basalt chemistry all change dramatically. We attribute this discontinuity and the contrasting characteristics of the supersegments to localized differences in the upper mantle thermal structure brought on by variable spreading geometry. The influence of these differences on the erupted composition of MORB appears to be more significant at ultraslow spreading rates where the overall degree of melting is lower. In contrast to the moderate and rather constant degrees of partial melting along the orthogonal supersegment, suppression of mantle melting on the oblique supersegment due to thickened lithosphere means that the bulk source is not uniformly sampled, as is the former. On the oblique supersegment, more abundant mafic lithologies melt deeper thereby dominating the more enriched aggregate melt composition. While much of the local major element heterogeneity can be explained by polybaric fractional crystallization with variable H_2O contents, elevated K_2O and K/Ti cannot. On the basis of the chemical and tectonic relationship of these enriched and depleted basalts, their occurrence requires a multilithology mantle source. The diversity and distribution of MORB compositions, especially here at ultraslow spreading rates, is controlled not only by the heterogeneity of the underlying mantle, but also more directly by the local thermal structure of the lithosphere (i.e., spreading geometry) and its influence on melting processes. Thus at ultraslow spreading rates, process rather than source may be the principle determiner of MORB composition.

Components: 21,174 words, 15 figures, 6 tables.

Keywords: MORB; ultraslow spreading; lithospheric thickness; melt focusing.

Index Terms: 1032 Geochemistry: Mid-oceanic ridge processes (3614, 8416); 1021 Geochemistry: Composition of the oceanic crust; 1065 Geochemistry: Major and trace element geochemistry.

Received 25 January 2008; **Revised** 19 February 2008; **Accepted** 21 February 2008; **Published** 15 May 2008.

Standish, J. J., H. J. B. Dick, P. J. Michael, W. G. Melson, and T. O'Hearn (2008), MORB generation beneath the ultraslow spreading Southwest Indian Ridge (9–25°E): Major element chemistry and the importance of process versus source, *Geochem. Geophys. Geosyst.*, *9*, Q05004, doi:10.1029/2008GC001959.

1. Introduction

[2] As the most abundant lavas on earth, mid-ocean ridge basalts (MORB) show significant compositional variation at both the regional "ocean basin" and local "ridge segment" scales. These variations often correlate with the composition of the residual abyssal mantle [e.g., *Dick and Fisher*, 1984], which together with theoretical [*Klein and Langmuir*, 1987; *McKenzie and Bickle*, 1988] and experimental work [e.g., *Baker and Stolper*, 1994; *Jaques and Green*, 1980; *Walter*, 1998] show that ocean ridge basalt is produced by partial melting of a peridotitic mantle. Ridges situated close to upwelling mantle plumes tend to erupt trace element and isotopically enriched lavas that are commonly attributed to the direct chemical influence of the mantle hot spots [*Schilling et al.*, 1983] and increased degrees of mantle melting [*Dick et al.*, 1984]. However, similarly enriched basalts are also erupted on ridges far from present-day hot spots, requiring various other explanations for their generation that include differences in mantle potential temperature and extent of melting [e.g., *Kinzler and Grove*, 1992; *Klein and Langmuir*, 1987; *Langmuir et al.*, 1992; *McKenzie and Bickle*, 1988], differences in regional mantle source composition [e.g., *le Roux et al.*, 2002b; *Meyzen et al.*, 2003; *Shen and Forsyth*, 1995], hydrous melting and differentiation [e.g., *Asimow and Langmuir*, 2003; *Gaetani and Grove*, 1998; *Michael and Chase*, 1987], prior source enrichment [e.g., *Donnelly et al.*, 2004; *Hanson*, 1977; *le Roux et al.*, 2002b], or variations in depth of mantle upwelling and melting related to ridge migration [*Small and Danyushevsky*, 2003]. However, it remains to be seen whether these regional-scale models can adequately explain segment-scale changes in basalt composition.

[3] The vast majority of MORB studies have focused on fast, intermediate, and slow spreading environments, whereas very few contributions (most are quite recent) have investigated the generation and composition of MORB along ultraslow spreading ridges (<20 mm/a). Yet investigation of these end-member ridges is critical to understand the relationship between spreading rate, crustal thickness, and MORB composition. At such slow spreading rates (both actual and effective), it is widely accepted that because of decreased mantle upwelling (i.e., lost heat by conduction) the lithosphere is thicker, leading to a shorter melting column and a decreased total volume of melt production [*Bown and White*, 1994]. As a result, crustal thickness drops off irregularly and dramatically [e.g., *Jokat et al.*, 2003; *Jokat and Schmidt-Aursch*, 2007; *Reid and Jackson*, 1981], often with significant effects on melt chemistry [*Ito and Mahoney*, 2004b] and tectonics [*Dick et al.*, 2003]. It is not surprising that recent studies of ultraslow spreading ridges have documented anomalous yet complementary morphologic, tectonic, geophysical, and geochemical features [e.g., *Cannat et al.*, 2003; *Dick et al.*, 2003; *Jokat et al.*, 2003; *Michael et al.*, 2003].

[4] One such example of an ultraslow spreading environment is the Southwest Indian Ridge (SWIR). The complex segmentation and variable spreading geometry, specifically between 9 and 25°E, provides a unique natural laboratory within which we investigate the erupted MORB compositions produced along one of the slowest spreading ridges far from any present-day hot spot influence. We report major element and water abundances from an extensive collection of MORB glasses that densely sample the 9–25°E portion of the SWIR. We discuss the correlations between the compositional range from N-MORB to E-MORB (based on K/Ti) and ridge characteristics such as,

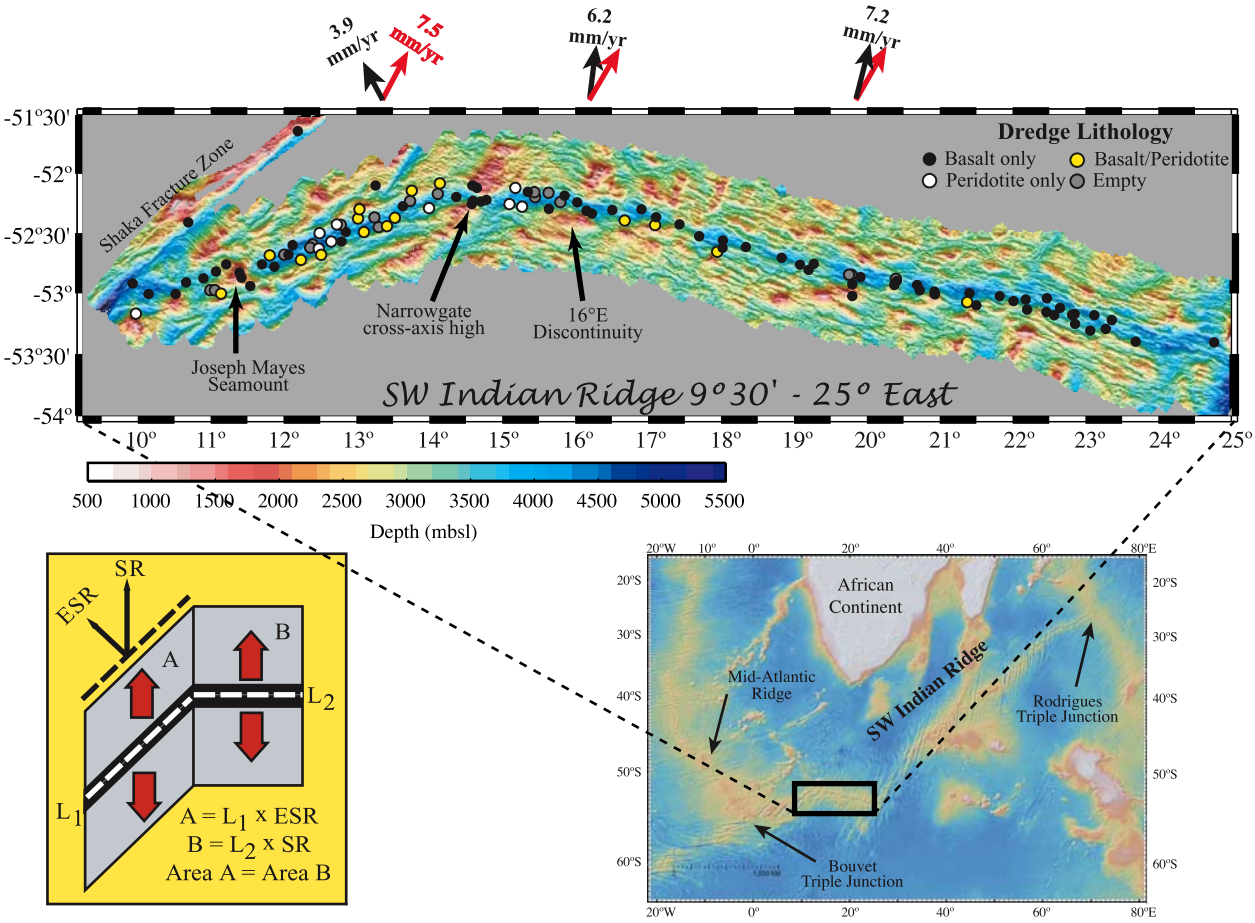

Figure 1. SWIR bathymetry, dredge location, and lithologic distribution. 9–16°E swath bathymetry combined with bathymetry from 16 to 25°E [*Grindlay et al.*, 1998]. Detailed dredge info available upon request. Lithologic rock type indicated by symbol color (see legend), with segment averaged statistics displayed in Tables 2a and 2b. Half spreading rate marked by red arrows and effective spreading rate (ESR) by black arrows, illustrating the local effect of increased ridge obliquity. Inset (left): cartoon depicting calculation of ESR. Lithospheric sections A and B have equal area, but segment length L1 > L2 thus, ESR < SR. ESR is component of spreading perpendicular to trend of ridge axis (i.e., mantle upwelling rate). Map inset (right): regional site map taken from http://www.geomapapp.org.

ridge morphology, spreading geometry, and crustal and lithospheric thickness. Our findings suggest that the variability in MORB chemistry is indeed a function of source heterogeneity, but is more significantly influenced by melting processes. The model we present illustrates the critical role that mantle thermal structure and lithospheric thickness play in determining the erupted compositions of MORB, specifically along slow and ultraslow spreading ridges.

2. Tectonic Ridge Characteristics

2.1. Regional Setting

[5] Situated between the African and Antarctic plates, the SWIR measures 7700 km in length and is one of the slowest spreading mid-ocean ridges with an average full rate of 14–15 mm/a [*Menke*, 2005]. Much of the SWIR has a highly oblique (~60°) SW-NE orientation (Figure 1, map inset) relative to the plate spreading direction, which is reflected in the dominance of numerous large transform offsets. These portions of the SWIR display typical slow spreading ridge segmentation, characterized by second-order magmatic segments [*Sinton et al.*, 1991] linked by transform offsets and smaller nontransform discontinuities. In contrast, our study area from 9 to 25°E (Figure 1) exhibits an E-W trend and, along with large portions of the eastern SWIR [*Cannat et al.*, 2006; *Sauter et al.*, 2004], lacks transforms; instead displaying orthogonal to suborthogonal magmatic accretionary segments linked by oblique amagmatic accretionary segments [*Dick et al.*, 2003].

[6] Within our study area, the ''orthogonal supersegment'' from 16°E to 25°E maintains an orthogonal to suborthogonal (<10° obliquity) angle to the spreading direction. It spreads on a series of magmatic accretionary segments that are linked by short nontransform offsets, not unlike the well-characterized slow spreading Mid-Atlantic Ridge [*Grindlay et al.*, 1998]. By contrast, the ''oblique supersegment'' from 9°E to 16°E has highly variable axial orientation relative to the spreading direction, containing segments that range from orthogonal to ~56° obliquity. This section of the SWIR takes on a very different appearance with alternating magmatic and amagmatic segments, where magmatism abruptly fluctuates and distinctive ultraslow spreading accretionary tectonics become stable [*Dick et al.*, 2003].

[7] Geometrically, as the obliquity of a ridge axis increases, so too does the ridge length per unit lithosphere created (Figure 1, inset). As a result, mantle upwelling must decrease proportionately to this added ridge length. The amount that mantle upwelling slows is calculated as the effective spreading rate, and defined as the spreading component perpendicular to the ridge axis. Studies of the effects of ridge obliquity on upwelling rate, lithospheric cooling, and crustal thickness [e.g., *Reid and Jackson*, 1981] are not new, and recent studies (Knipovich Ridge [*Okino et al.*, 2002]; SWIR/Gakkel Ridge [*Dick et al.*, 2003]; Lena Trough [*Snow et al.*, 2004]) have continued to debate the impact of spreading geometry on magmatic and tectonic segmentation style. On the basis of these recent observations, *Dick et al.* [2003] suggested that the transition from slow spreading tectonics to ''ultraslow spreading accretionary ridge tectonics,'' where linked magmatic and amagmatic accretionary segments replace transform faults, occurs at an effective spreading rate of ~12 mm/a or less (full rate).

[8] In this manuscript, we restrict ultraslow spreading ridges to the portion of the global ridge system with a full spreading rate below 20 mm/a. We note, however, that the rate at which a ridge diverges does not exclusively determine its morphologic, tectonic, or geochemical characteristics; fast, slow, and ultraslow spreading ridges alike can, and often do, display variable ridge characteristics. It is possible to have slow spreading accretionary tectonics on a ridge spreading at <20 mm/a, whereas ultraslow spreading accretionary tectonics appear to be stable only at spreading rates ≤12 mm/a. In this way, a spreading rate below 20 mm/a is a necessary but not sufficient reason for ultraslow spreading ridge accretionary tectonics to occur.

2.2. Local Tectonic Provinces

[9] The transition in ridge orientation at 16°E also marks an abrupt change in ridge morphology, physiography, lithology, and segmentation pattern, thereby providing a logical division between the orthogonal and oblique supersegments. While the orthogonal supersegment displays rather consistent ridge characteristics, the oblique supersegment contains three significantly diverse ridge sections. Thus, within the study area we designate four distinct tectonomagmatic provinces: (1) the orthogonal supersegment, (2) the oblique amagmatic accretionary segments, (3) Narrowgate magmatic segment, and (4) Joseph Mayes Seamount, the latter three of which comprise the oblique supersegment. Table 1 summarizes the ridge characteristics for each of these provinces, which are discussed in detail below.

2.2.1. Orthogonal Supersegment

[10] The 630 km long orthogonal supersegment (Figure 2; 15°45′–25°E) displays typical slow spreading ridge morphology and geology. Two nearly orthogonal sections, 290 and 220 km long respectively, are linked by a slightly more oblique (~10°) 120 km long section between 20° and 22°E [*Grindlay et al.*, 1998]. The entire province is characterized by fourteen short (10–15 km) to moderate length (20–35 km) second-order magmatic segments [*Grindlay et al.*, 1998] (Figure 2), with dominantly left stepping, en echelon segmentation accommodated by short (<10 km) nontransform offsets. Despite a noticeable increase in ridge obliquity between 15 and 16°E, the individual magmatic segments maintain a perpendicular orientation to spreading direction, as the offset between segments increase. As a result, effective spreading rates for the individual magmatic segments are similar to the average supersegment full spreading rate (~14.5 mm/a).

[11] Rift mountain topography along the supersegment is rough but relatively symmetrical about the spreading axis (Figure 2b). The cross-axis profiles show similar total rift valley relief of 1500–2000 m (measured from the valley floor to the crest of the bounding wall), and the distinctive staircase normal faulting characteristic of slow spreading ridges. Twelve magmatic segments are topographically elevated at their midpoints with the rest showing irregular, asymmetrical along-axis segment profiles

Table 1. Representative Ridge Characteristics for Each Tectonomagmatic Province

Ridge Characteristics[a]	Orthogonal Supersegment	Amagmatic Accretionary Segments[b]	Joseph Mayes Seamount	Narrowgate Segment
Longitudinal location, °E	15°45′–25°06′	see footnotes	11°–11°35′	14°15′–14°54′
Average axial depth, m	3796 ± 374	4151 ± 425	2574 ± 711	3532 ± 295
Spreading rate,[c] mm/a full rate	14.4 ± 0.1	14.1 ± 0.1	14.1 ± 0.1	14.2 ± 0.1
Effective spreading rate,[d] mm/a	14.3 ± 0.5	9.1 ± 2.1[e]	13.3 ± 0.1	14.2 ± 0.1
Rift valley width, km	28.8 ± 1.5	40.8 ± 11.5	67.5[f]	18.3
Inner valley floor width, km	13.7	10.6	-	8.8
Cross-axis relief, km	2.5	2.4	2.6[g]	1.7
Number of segments	14	4	1	1
Segment length, km	42 ± 15	~100	~50	35

[a] Data are compiled from profiles presented in Figure 2 and 4; orthogonal supersegment and amagmatic accretionary segment data is averaged.
[b] Three segments comprise this tectonomagmatic province: 9°30′–11°E, 11°35′–14°15′E, and 14°54′–15°45′E.
[c] Full spreading rate and FSR azimuth calculated at http://www.ldeo.columbia.edu/users/menke/plates.html.
[d] ESR calculated following the method of *Abelson and Agnon* [1997], with ESR azimuth measured by hand.
[e] Average value for all three segments; does not include the segment west of JMS because of unconstrained rift valley boundaries and morphology.
[f] Measured from northern bounding peridotite block to southern bounding block.
[g] Taken from *x* axis profiles (Figure 2) Total relief for JMS (measured from adjacent rift valley deep to crest of JMS) is ~3.9 km.

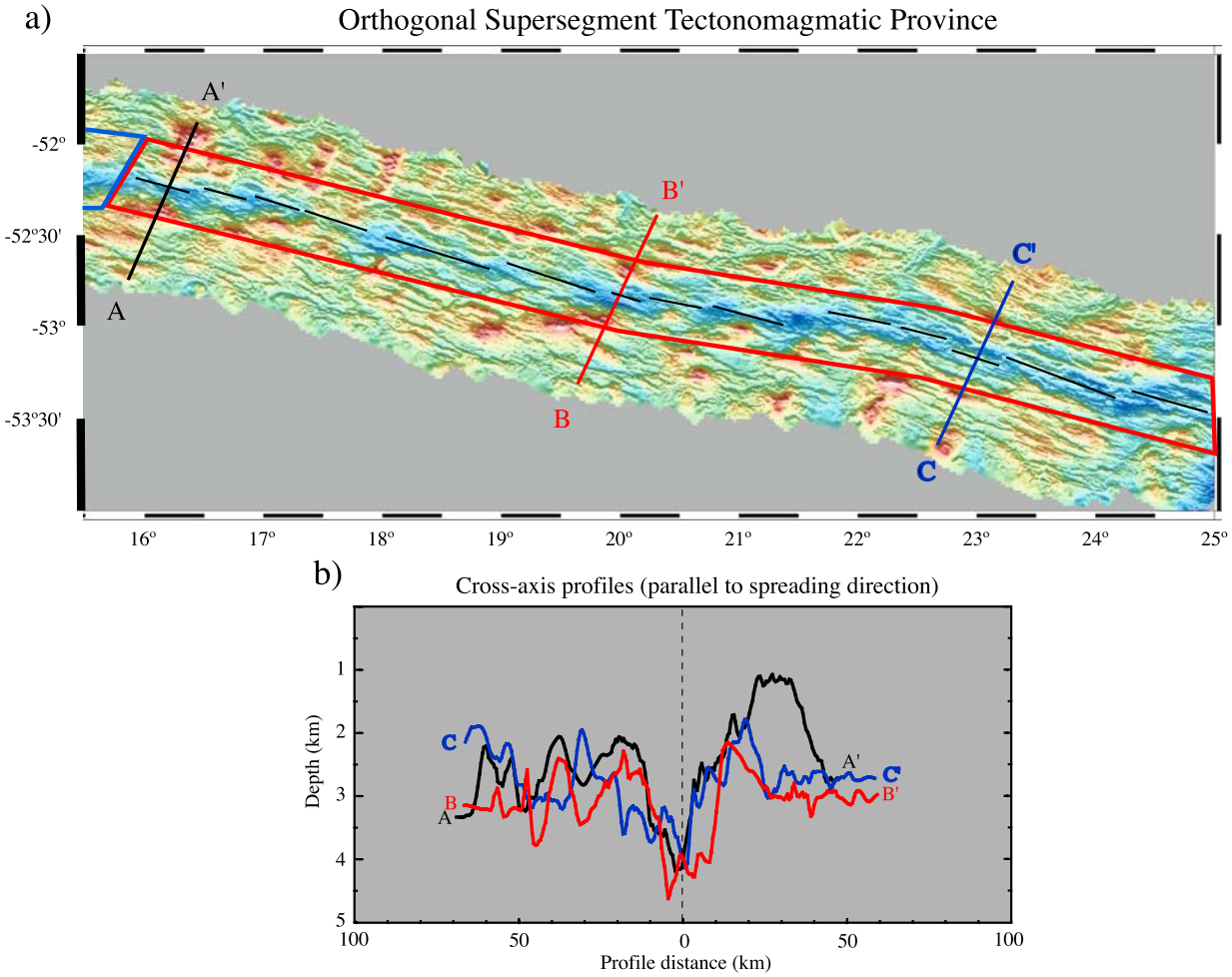

Figure 2. Bathymetry and cross-axis topographic profiles for the orthogonal supersegment tectonomagmatic province (~15°45 to 25°E). (a) Supersegment is devoid of transform offsets and contains fourteen magmatic spreading segments [*Dulaney*, 2002; *Grindlay et al.*, 2000], delineated by thin black lines and linked by small nontransform offsets. (b) Cross-axis profiles (A-A′, B-B′, and C-C′) taken parallel to spreading direction, show similar along-axis rift mountain symmetry, but variable rift valley morphology. V.E. = 40:1.

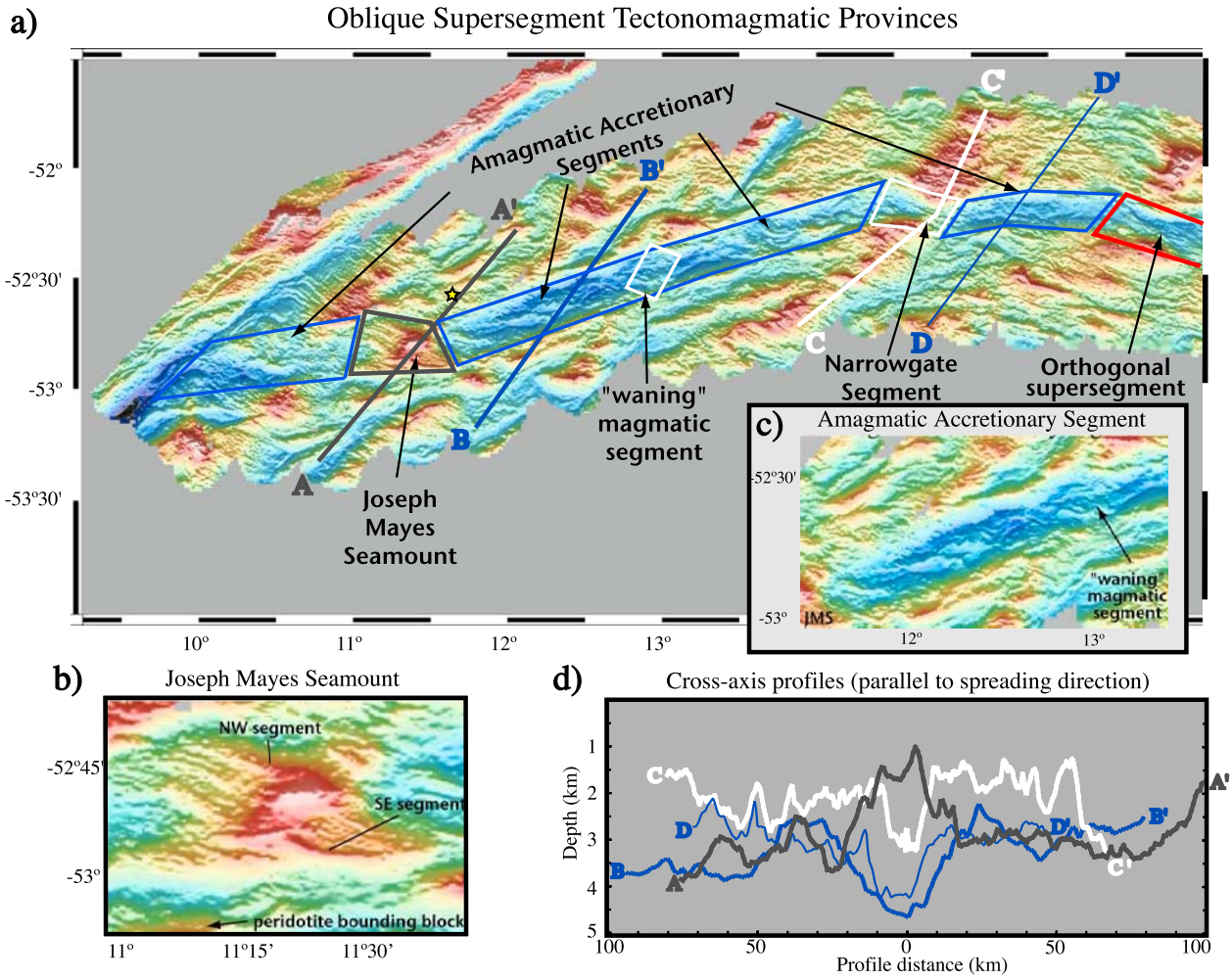

Figure 3. Bathymetry and cross-axis topographic profiles for the oblique supersegment (9–16°E). (a) Oblique supersegment bathymetry consists of three tectonomagmatic provinces: (1) Joseph Mayes Seamount at 11°20′E outlined in gray; (2) the amagmatic accretionary segments (west of JMS, between JMS and Narrowgate segments, and east of Narrowgate segment) outlined in blue (the "waning" magmatic segment (white) at ~12°50′E is part of this tectonomagmatic province); and (3) Narrowgate segment at 14°41′E outlined in white. Yellow star indicates location of piston core sample IO 11/76-76-1, which recovered serpentinite. (b) Joseph Mayes Seamount illustrating dual peaks with associated segments extending to the SE and NW. (c) Central amagmatic accretionary segment between JMS and 13°E, which includes the "waning" magmatic segment. (d) Cross-axis profiles for each tectonomagmatic setting. Profiles are parallel to spreading direction (for profiles B and D that is ~52° oblique to axis). Narrowgate profile (C-C′) follows bathymetric high on south side of ridge. V.E. = 40:1.

[*Dulaney*, 2002]. The majority of the segments display linear axial volcanic ridges; indicating melt flow is focused to a narrow zone along the rift axis.

2.2.2. Amagmatic Accretionary Segments

[12] Three "amagmatic" accretionary segments exist within the oblique supersegment: 9°30′–11°E, 11°35′–14°15′E, and 14°54′–15°45′E (Figure 3). They are termed "amagmatic" rather than "avolcanic" to reflect the abundant peridotite, scattered basalt, minimal diabase, and virtual absence of gabbro recovered in these areas. This is in contrast to similarly anomalous spreading segments such as those near the 15°20′ F.Z. on the MAR, which may be better termed "avolcanic," as extensive dredging and drilling recovered a high percentage of gabbro (30–40%) along with abundant mantle peridotites, suggesting that the total volume of melt emplaced to the lithosphere may be similar to that of more typical magmatic segments [*Fujiwara et al.*, 2003; *Kelemen et al.*, 2007]. Amagmatic segments are a unique tectonomagmatic setting and an integral part of ultraslow spreading ridge tectonics. They are a new class of plate boundary structure that can assume any

orientation to the spreading direction and replace both transform faults and accretionary magmatic segments [*Dick et al.*, 2003].

[13] Each of the amagmatic segments acts as a linking accretionary segment between more magmatically robust orthogonal spreading segments. Two amagmatic segment profiles have rift valley relief similar to profiles on the orthogonal supersegment, but with valley floors ~500 m deeper (Figure 3d). Profile B-B′ has a wide rift valley (>50 km, peak to peak) and inner valley floor (19.5 km wide), gently sloping walls, and relatively subdued rift mountain topography. Profile D-D′ has a narrower rift valley (29 km) and inner rift valley (12.5 km), steeper rift valley walls, and heavily faulted rift mountain topography. Comparison of these cross-axis profiles illustrates the significant variability in ridge morphology within this tectonomagmatic province. We attribute the gently dipping nature of the rift valley walls in profile B-B′ to low-angle faults exposing massive peridotite blocks. The recovery of peridotites proximal to B-B′ and D-D′ suggests we may be seeing two different stages of mantle exposure. In this case, the narrower rift valley and steeper slopes of D-D′ could reflect an early stage of high-angle extension and faulting that is unroofing the oceanic mantle. Not unexpectedly, the morphology of these segments and the character of the rift valley floor show the unorganized nature of volcanism.

[14] One exception is observed near the center of the prominent 11°35′–14°15′E amagmatic segment that links the Narrowgate and Joseph Mayes Seamount magmatic segments. Here, a short, inconspicuous suborthogonal 22 km long magmatic segment centered at 12°55′E (Figure 3c) displays a 25 km wide rift valley containing several suborthogonal volcanic ridges that yielded fresh to moderately weathered glassy pillow basalts. It has a small <15 mGal negative mantle Bouguer anomaly and ~5 Am/m positive magnetic anomaly, both much less robust than observed at the Joseph Mayes Seamount and Narrowgate volcanic centers (see below) [*Dick et al.*, 2003]. Topographically elevated rift mountains associated with this segment center increase in along-axis length and width with distance off-axis (Figure 3c), suggesting the present-day segment is vestigial of a previously robust magmatic segment.

2.2.3. Narrowgate Segment

[15] Narrowgate segment (14°15′–14°54′E; Figure 3a) is a volcanically robust, orthogonal spreading segment with a 2700 m deep and 20 km wide rift valley. The shoaling of the neovolcanic zone and narrowing of the rift valley with respect to the neighboring amagmatic segments creates a noticeable constriction in the rift valley morphology and is thus a distinguishing feature of this province. Despite flanking oblique spreading amagmatic segments, Narrowgate segment is oriented nearly perpendicular to the spreading direction with an effective spreading rate of 14.2 mm/a full rate. The cross-axis profile C-C′ at the midpoint of the neovolcanic zone (Figure 3d) shows similar morphology in the rift mountains to either side, suggesting symmetric spreading. Rift valley relief on profile C-C′ is ~1500 m and the inner rift valley width is only 8–9 km, noticeably narrower than other provinces (see Table 1). We observe a 45 km long axial volcanic ridge with its bathymetric high point in the center of the segment. Combined with a measured 20–30 mGal negative bull's eye, a +15 Am/m magnetic anomaly, and the recovery of abundant fresh glassy pillow basalts, this strongly suggests robust and possibly focused volcanism.

[16] A cross-axis volcanic plateau forming a V-shaped trace subparallel (5° to 15°) to the spreading direction extends ~100 km into the rift mountains to the NNE and at least 200 km to the SW, suggesting robust magmatic activity for at least 8–9 Ma. Similarly elevated rift mountain terrain occurs along the orthogonal supersegment, with visible V-shaped ridges at 16°E and 20.3°E [*Grindlay et al.*, 1998] (segments 1 and 8).

2.2.4. Joseph Mayes Seamount

[17] Joseph Mayes Seamount, located between 11 and 11°35′E, is perhaps the largest non–hot spot volcano on the global ridge system (Figure 3a). It is a sigmoidally shaped point source axial volcano with two prominent limbs that curve to the west and east respectively to join with the northern and southern walls of the adjacent amagmatic rifts. The seamount rises from the amagmatic trough at 4500 m to within 1000 m of the sea surface, prominently displaying a double peaked axial summit (Figure 3b). It is bounded to the north and south by a split preexisting peridotite block inferred from dredging, morphology, gravity, and magnetics to have been rifted 20 km apart by the volcano (Figure 3b; also visible from profile A-A′ in Figure 3d). On the basis of the orientation of the summit axial ridges, Joseph Mayes Seamount is spreading suborthogonally, with an effective spreading rate just over 13 mm/a (full rate). Using this rate and the separation distance between the

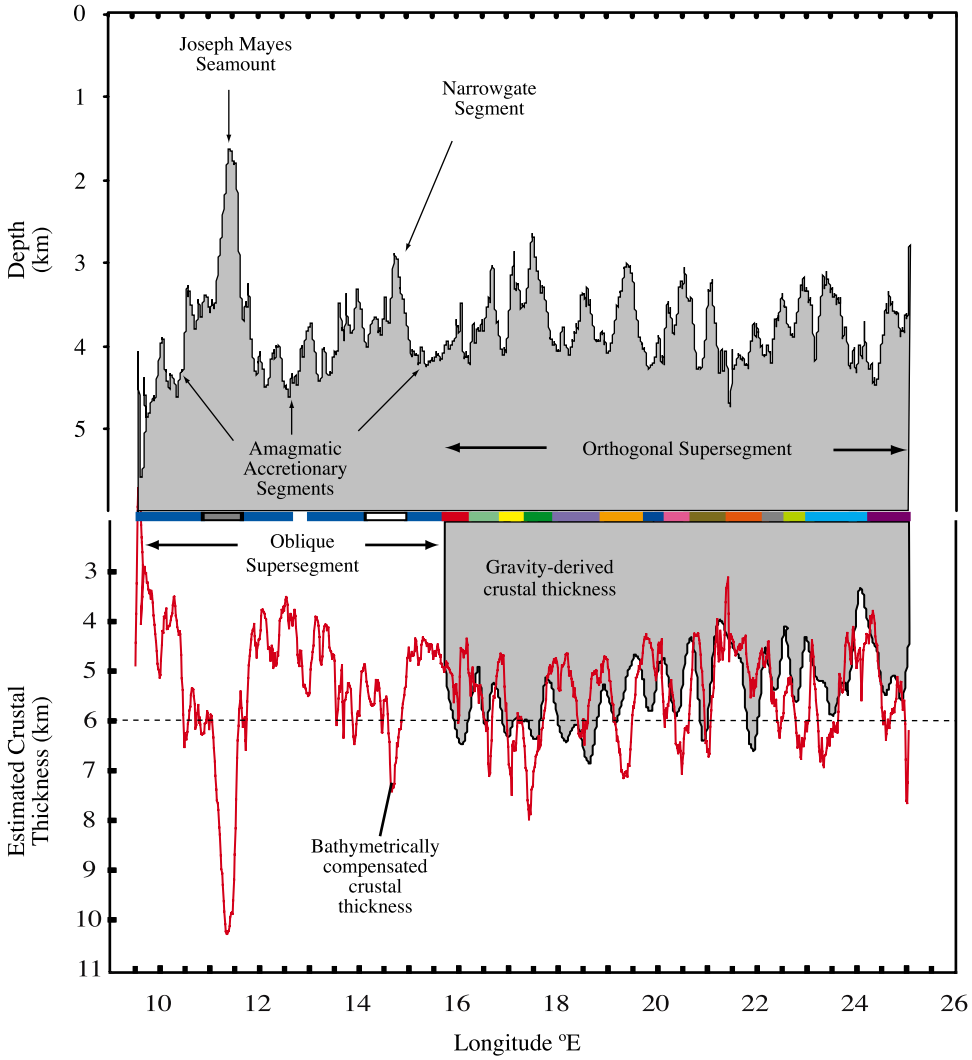

Figure 4. Along-axis bathymetry and estimated crustal thickness profile for SW Indian Ridge (9–25°E). Gravity-derived crustal thickness (gray field) [*Dulaney*, 2002; *Grindlay et al.*, 2000] is not unique and is modeled relative to a 6 km thick oceanic crust. Isostatically compensated (i.e., Airy) crustal thickness is calculated assuming crustal, mantle, and seawater densities of 2750, 3300, and 1030 kg m^{-3}, respectively. Agreement between isostatically compensated and gravity-derived crustal thickness on the orthogonal supersegment indicates full isostatic compensation. Variations in crustal thickness along the oblique supersegment are significant for each of the three tectonic provinces when compared to the orthogonal supersegment. Colored bars denote segmentation, where segmentation on the orthogonal supersegment is taken from Figure 2, and segmentation on the oblique supersegment is marked as Narrowgate segment (white), Joseph Mayes Seamount (gray), amagmatic accretionary segments (blue), with the main amagmatic segment between JMS and Narrowgate segment separated by a "waning" magmatic segment.

peridotite blocks, the volcano is less than 1.3 Ma old. Volcanic activity has occurred along the entire 50 km segment length, as illustrated by multiple NW and SE trending ridges that extend from the two peaks.

2.3. Crustal Thickness

[18] Along-axis estimated crustal thickness estimated from gravity [*Dulaney*, 2002; *Grindlay et al.*, 2000] is not constant across the study area and shows significant variations between tectonomagmatic provinces. The orthogonal supersegments' bathymetric profile displays numerous segment centers ~1000 m shallower than their segment ends, but with little change in the depth of the segment high point (~3025 m). Despite this somewhat monotonous bathymetry profile, both gravity-derived and Airy compensated crustal thickness

Table 2a. Dredge Averaged Statistics Compiled From Sample Descriptions[a]

		Dredged Rock Lithologies[b]							
Ridge Province	Location	Weight, kg	Pillow Basalt and Basalt	Peridotite and Dunite	Gabbro	Diabase	Hawaiite	Hydrothermal and Volcanoclastics	Sedimentary Rocks and Erratics
Oblique supersegment	9°56′–15°45′E								
Amagmatic segments	9°56′–11°E; 11°36′–14°15′E; 14°54′–15°45′E	3511.7	39.2%	43.7%	1.6%	1.9%	0.4%	7.3%	6.0%
Rift mountains north and south of Joseph Mayes Seamount (D29 and D30)		109.0	39.3%	55.9%	0.0%	0.0%	0.0%	0.0%	4.9%
Joseph Mayes Seamount (excluding D29 and D30)	11°–11°36′E	317.7	96.7%	0.0%	0.0%	2.0%	0.0%	0.3%	1.0%
Narrowgate segment	14°15′–14°54′E	1119.1	67.0%	0.0%	0.0%	20.6%	0.0%	10.5%	1.9%
Oblique supersegment averages (all dredges)		**5057.5**	**49.0%**	**31.5%**	**1.1%**	**6.0%**	**0.3%**	**7.4%**	**4.7%**
Orthogonal supersegment	**15°45′–25°E**	**4044.8**	**85.5%**	**4.2%**	**3.2%**	**5.0%**	**0.0%**	**1.6%**	**0.4%**
All dredge averages		9102.3	65.2%	19.4%	2.0%	5.6%	0.1%	4.8%	2.8%

[a] Descriptive information (i.e., phenocryst %, vesicle %) was reviewed at sea by the authors to ensure consistency and minimize error. Statistics were generated from 125 dredge locations of which 105 successfully recovered material, including 1 ARA *Islas Orcadas*, 13 SA *Agulhas*, 8 R/V *Polar Stern*, 70 R/V *Knorr*, and 33 R/V *Melville* dredges. In addition, there is one *Islas Orcadas* rift mountain serpentine core and one *Melville* rift valley sediment core. Detailed descriptions of our techniques and methods for bathymetric data collection, dredging operations, and sample cataloging are contained in the auxiliary material.

[b] Dredged rock lithologies, mass of rock in kilograms which falls into each general lithologic classification.

measurements indicate a modest yet steady east to west increase in crustal thickness. From 25 to 16°E estimated crustal thickness values vary at the segment scale and display ~1.5 km of thickening (Figure 4).

[19] On the oblique supersegment, bathymetry and crustal thickness vary much more erratically. The amagmatic segments are some of the deepest ridge sections, corresponding to some of the thinnest crust, particularly between Joseph Mayes Seamount and Narrowgate segment, where the crustal thickness approaches ~4 km. Narrowgate segment crust is 7.5 km thick, and thus is ~1 km thicker than the western end of the orthogonal supersegment (Figure 4). The other volcanically robust segment, Joseph Mayes Seamount, has 10 km thick crust and is substantially thicker than any other segment in the study area. These along-axis variations in crustal thickness may be explained by either local variations in melt generation or along-axis focusing and redistribution of melt, or both. Notably, the oblique supersegment contains both the thickest and thinnest crust of our study area, and not coincidentally also the segments with the greatest obliquity. Significant thinning of the crust in the amagmatic segments relative to the surrounding magmatic segments supports the possibility of thin to locally absent basaltic crust [*Dick et al.*, 2003]. Yet even where magmatic crust may be entirely absent, as suggested by proximal dredge hauls of mantle peridotite only, and the relative scarcity of gabbro (statistics in section 4.1), a nonzero crustal thickness calculated from gravity may be due to serpentinization of the shallow mantle [e.g., *Cannat et al.*, 2003; *Mével*, 2003].

3. Dredge Data and Chemical Results

3.1. Lithologic Distribution

[20] Dredge recovery statistics for 105 successful dredges from 5 cruises to 9–25°E show significant lithologic differences (i.e., peridotite versus gabbro versus basalt) between the two supersegments, and

specifically between the tectonomagmatic provinces within the oblique supersegment (Table 2a). There was a disproportionate number of empty dredge hauls on the oblique supersegment (specifically the amagmatic segments) compared to the orthogonal supersegment, which we interpret to indicate a localized absence of basaltic crust (see auxiliary material for further discussion).[1] This together with an increased abundance of peridotite on the amagmatic segments relative to the other tectonomagmatic provinces, implies significant thinning of the basaltic crust and supports the crustal thickness findings. Detailed lithologic descriptions are compiled in Table 2a and auxiliary material Table S1.

3.2. Basalt Phenocryst and Vesicle Content

[21] Significant differences in vesicularity, phenocryst content, and phenocryst assemblage exist between the tectonomagmatic provinces (Table 2b). As most vesicles are small, and not readily distinguishable to the naked eye, vesicularity was always estimated using a hand lens.

[22] In general, lavas from the orthogonal supersegment have low but measurable vesicle content. A small but noticeable gradient in the range of vesicularity is observed, as basalts on the eastern end have 2–3% vesicularity, while those to the west have up to 7% vesicularity. Oblique supersegment basalts display a large range in vesicularity and phenocryst abundance between the tectonomagmatic provinces, with Narrowgate segment and Joseph Mayes Seamount lavas consistently having the highest vesicularity and moderate phenocryst abundances. The amagmatic segment lavas generally have greater phenocryst abundance, but low to moderate vesicularity. The difference in vesicularity between supersegments is consistent with higher average water contents in the oblique supersegment lavas (see next section). This relationship generally holds for lavas within the oblique supersegment, as the Narrowgate segment and Joseph Mayes Seamount lavas have higher average water contents and vesicularity than the amagmatic segment lavas.

[23] All four tectonomagmatic provinces are dominated by Ol only and Ol + Plag phenocryst assemblages, with sparse (<4% of lavas) or absent Cpx (Table 2b). Basalts from the orthogonal supersegment are dominated by Plag-phyric basalts (57%), while Ol-Plag-phyric basalts are most abundant along the oblique supersegment (48%). In addition, the oblique supersegment basalts are substantially more phenocryst rich than the orthogonal supersegment basalts. These differences likely reflect differences in magmatic processes and melt transport in the crust.

3.3. Dissolved Water and Carbon Dioxide Abundance

[24] Total dissolved H_2O concentrations range from 0.15 to 1.04 wt % and CO_2 concentrations range from 141 to 256 ppm (Table 3). Dissolved water contents are variable but largely cluster according to tectonomagmatic province, with the orthogonal supersegment lavas having the lowest abundances and Narrowgate segment lavas the highest (Figure 5a). CO_2 contents are similar for all provinces, and because of degassing show no local or regional correlations with H_2O or anything else (Figure 5a). Equilibration pressures and vapor compositions (Figure 5a) for each glass were calculated on the basis of the solubility model of *Dixon et al.* [1995]. Southwest Indian Ridge glasses have equilibration pressures between 330 and 550 bars, corresponding to vapor compositions with H_2O fractions "X_{H2O}" between 0.004 and 0.264. The majority of the glasses have X_{H2O} less than 0.1. Calculated equilibration pressures plotted versus estimated eruption pressures (depth at the start of the dredge) in Figure 5b show nearly all glasses to be supersaturated, and since the majority of the glasses are from the rift valley floor these values likely represent maximum eruption pressures. Of the 40 glasses measured, only 7 are from outside the rift valley (all on the oblique supersegment), where tectonic uplift may have moved these lavas to depths shallower than their initial eruption depths. Variable vesicle contents (Table 2b) plus supersaturation of nearly all the glasses in Figure 5b (above the 1:1 line) means the lavas were degassing upon eruption. However, because H_2O has a greater solubility than CO_2 in basaltic melts at low pressures [*Dixon et al.*, 1995; *Dixon and Stolper*, 1995], the vapor compositions in equilibrium with these lavas were CO_2 rich (Figure 5a). Therefore, any preeruptive degassing was dominated by CO_2 loss, with only a small proportion of the vapor being H_2O. To verify this (especially for highly vesicular glasses), we took the calculated vapor compositions [*Dixon and Stolper*, 1995] together with the dredge averaged intrinsic vesic-

[1] Auxiliary materials are available in the HTML. doi:10.1029/2008GC001959.

Table 2b. Summary of Dredged Basaltic Rocks

Tectonomagmatic Province	Lithology		Phenocryst Volume				Phenocryst Assemblages						Vesicularity			
	Basalt and Diabase	Pillow Basalt	>10% Phenocryst	2–10% Phenocryst	<2% Phenocryst	Aphyric	Ol Phyric	Pl-Ol Phyric	Pl Phyric	Ol-Cpx Phyric	Pl-Cpx Phyric	Pl-Ol-Cpx Phyric	>10% Vesicularity	2–10% Vesicularity	<2% Vesicularity	No Vesicularity
16–25°E orthogonal supersegment																
16–25° rift valley axis	453	1643	53	832	530	748	146	343	915	0	0	0	48	960	339	805
21 dredges, 2096 kg	21.6%	78.4%	2.5%	38.4%	24.5%	34.6%	10.4%	24.4%	65.2%	0.0%	0.0%	0.0%	2.2%	44.6%	15.7%	37.4%
16–25° rift valley walls	1222	818	90	509	275	1015	66	429	443	0	3	2	59	702	473	567
20 dredges, 2040 kg	59.9%	40.1%	4.8%	26.9%	14.5%	53.7%	7.0%	45.5%	47.0%	0.0%	0.4%	0.2%	3.3%	39.0%	26.3%	31.5%
16–25° supersegment	1675	2461	144	1341	805	1763	212	773	1358	0	3	2	107	1662	812	1372
41 dredges, 4136 kg	**40.5%**	**59.5%**	**3.5%**	**33.1%**	**19.9%**	**43.5%**	**9.0%**	**32.9%**	**57.8%**	**0.0%**	**0.1%**	**0.1%**	**2.7%**	**42.1%**	**20.5%**	**34.7%**
10–16°E oblique supersegment																
15–16°E amagmatic trough, 4 dredges 179 kg	2.4	0.0	0.5	0.0	0.0	0.0	1.9	0.5	0.0	0.0	0.0	0.0	0.5	0.0	0.0	0.0
Narrowgate magmatic center	250	435	13	423	131	118	99	330	127	1	8	2	276	318	77	13
5 dredges, 1178 kg	**36.5%**	**63.5%**	**1.9%**	**61.8%**	**19.2%**	**17.2%**	**17.5%**	**58.3%**	**22.4%**	**0.2%**	**1.3%**	**0.4%**	**40.4%**	**46.5%**	**11.2%**	**1.9%**
11°30′–14°30′ axial trough	415	468	222	488	52	128	112	296	296	17	2	27	150	414	140	178
14 dredges, 2107 kg	47.0%	53.0%	25.0%	54.8%	5.8%	14.4%	15.0%	39.5%	39.5%	2.3%	0.3%	3.5%	17.0%	47.0%	15.9%	20.1%
Joseph Mayes Seamount	76	332	186	61	36	109	0	277	53	0	0	0	162	206	16	5
5 dredges, 423 kg	**18.6%**	**81.4%**	**45.5%**	**15.0%**	**8.9%**	**26.8%**	**0.0%**	**83.8%**	**16.2%**	**0.0%**	**0.0%**	**0.0%**	**39.8%**	**50.4%**	**4.0%**	**1.3%**
10–11°E amagmatic segment	183	236	36	241	23	119	102	129	76	0	0	0	13	185	73	149
7 dredges, 567 kg	43.69%	56.31%	8.5%	57.5%	5.6%	28.5%	33.1%	42.1%	24.8%	0.0%	0.0%	0.0%	3.0%	44.1%	17.5%	35.5%
10–16°E amagmatic segments	601	705	258	730	75	248	216	426	372	17	2	27	163	599	213	327
25 dredges, 2853 kg	**46.0%**	**54.0%**	**19.7%**	**55.7%**	**5.7%**	**18.9%**	**20.4%**	**40.2%**	**35.1%**	**1.6%**	**0.2%**	**2.5%**	**12.5%**	**46.0%**	**16.4%**	**25.1%**
Northern Cratered Plateau[a]																
Dredge 91, 52.093°S, 13.267°E, 2810 m	72.2	0.0	48.1	3.3	0.5	20.4	0.0	25.4	21.5	0.0	0.0	5.0	1.8	16.1	31.1	23.3
Shaka Ridge (121.0 kg basalts)[a]																
Dredge 1, 51.626°S 12.174°E, 2320 m	0.0	0.1	0.0	0.1	0.0	0.0	0.0	0.0	0.0	0.0	0.0	0.1	0.0	0.0	0.0	0.0
Dredge 27, 52.403°S 10.696°E, 2880 m	120.9	0.0	61.2	45.1	8.7	5.9	0.0	0.0	115.1	0.0	0.0	0.0	5.5	42.3	20.6	52.5

[a] Not included in statistics.

Table 3. Representative Glass Major Element, H_2O, and CO_2 Concentrations From Dredges Between 9 and 25°E on SW Indian Ridge

Sample Number[a]	Latitude	Longitude	Depth	SiO_2	Al_2O_3	FeO*	MgO	CaO	Na_2O	K_2O	TiO_2	P_2O_5	MnO	H_2O	CO_2[b]	Mg#[c]	CaO/Al_2O_3	K/Ti
Oblique supersegment (9°56′–15°45′E)																		
Amagmatic segments (9°56′–11°E; 11°36′–14°15′E; 14°54′–15°45′E)																		
VAN7-96-28	−53.140	9.979	3134	49.60	16.53	8.78	7.33	10.92	3.48	0.49	1.83	0.25	0.17			63.67	0.66	0.37
KN162-7 28-15	−52.896	10.674	3635	49.66	16.19	9.03	6.84	10.05	3.77	0.48	2.08	0.34	0.12			61.36	0.62	0.32
VAN7-92-03	−52.855	10.888	3700	49.67	15.43	9.83	6.34	11.00	3.58	0.61	1.94	0.21	0.19	0.64	192	57.50	0.71	0.44
KN162-9 30-06	−52.994	11.157	3536	48.65	17.77	9.09	8.93	11.43	2.63	0.25	1.06	0.12	0.16			67.34	0.64	0.33
KN162-9 30-12	−52.994	11.157	3536	49.90	16.48	8.64	8.02	11.60	2.80	0.42	1.45	0.22	0.15	0.35	173	66.08	0.70	0.40
KN162-9 36-27	−52.749	11.711	3981	50.32	16.64	8.36	7.77	10.37	3.91	0.21	1.69	0.21	0.18	0.34	165	66.09	0.62	0.17
KN162-9 38-21	−52.777	11.854	3964	50.47	16.20	9.37	7.10	10.12	3.40	0.57	1.74	0.29	0.19			61.37	0.62	0.45
KN162-9 41-07	−52.589	12.132	4333	50.23	15.57	9.41	6.57	10.65	3.70	0.54	2.10	0.34	0.18	0.61	230	59.41	0.68	0.36
KN162-9 48-04	−52.560	12.799	3897	49.13	17.75	8.00	9.07	11.84	3.15	0.08	1.06	0.10	0.16	0.18	246	70.41	0.67	0.10
KN162-9 49-13	−52.296	12.861	4199	49.89	17.37	7.00	8.38	10.92	3.40	0.53	1.41	0.23	0.14	0.49	192	71.52	0.63	0.52
KN162-9 51-11	−52.293	13.062	2233	49.99	17.32	7.26	8.59	11.53	3.12	0.31	1.35	0.17	0.17			71.28	0.67	0.32
PS4-06-01	−52.350	13.130	4000	51.81	16.45	7.62	7.12	10.11	3.66	0.89	1.71	0.30	0.11			66.19	0.61	0.72
KN162-9 53-01	−52.475	13.144	4222	49.93	16.92	8.19	6.84	10.55	3.93	0.59	1.77	0.26	0.17			63.65	0.62	0.46
VAN7-91-34	−52.093	13.267	3078	49.71	16.77	9.51	8.13	10.16	3.03	0.43	1.77	0.24	0.20	0.62	149	64.21	0.61	0.34
KN162-9 56-88	−52.370	13.506	4132	51.33	16.88	7.28	6.92	10.35	3.35	0.89	1.56	0.29	0.12	0.68	158	66.60	0.61	0.79
PS4-05-36	−52.280	13.680	3800	51.18	16.46	7.78	7.73	10.41	3.73	0.41	1.50	0.26		0.40	173	67.58	0.63	0.38
Joseph Mayes Seamount (11°–11°36′E)																		
KN162-9 31-01	−52.805	11.082	3184	49.99	15.42	9.68	6.58	10.91	3.52	0.48	1.95	0.30	0.19	0.54	152	58.76	0.71	0.34
KN162-9 32-09	−52.749	11.218	2664	50.15	15.06	10.57	6.11	10.35	3.61	0.56	2.04	0.31	0.19	0.60	163	54.82	0.69	0.38
KN162-9 33-49	−52.817	11.387	1436	50.44	15.15	10.39	5.48	9.35	3.99	0.83	2.38	0.44	0.22	0.77	197	52.49	0.62	0.48
KN162-9 34-23	−52.857	11.430	2070	50.05	15.66	9.23	6.98	11.37	3.46	0.57	1.76	0.28	0.17	0.62	199	61.31	0.73	0.45
KN162-9 35-03	−52.927	11.555	2555	49.99	14.77	10.98	5.19	9.52	4.20	0.76	2.39	0.39	0.24			49.81	0.64	0.44
Narrowgate segment (14°15′–14°54′E)																		
VAN7-90-77	−52.177	14.353	3973	48.75	16.20	7.94	7.95	13.28	2.80	0.51	1.46	0.35	0.15	0.44	216	67.75	0.82	0.48
PS4-03-14	−53.120	14.500	3300	50.84	16.17	8.99	5.79	7.95	5.03	1.47	1.85	0.45		0.92	181	57.46	0.49	1.10
VAN7-89-02	−52.246	14.598	2439	47.96	16.81	7.87	6.93	11.99	3.25	1.34	1.73	0.31	0.15	0.81	199	64.89	0.71	1.07
KN162-9 61-71	−52.104	14.601	2211	51.00	16.13	9.80	4.43	8.25	4.45	1.66	2.56	0.62	0.20	1.04	142	48.66	0.51	0.90
PS4-02-01	−52.220	14.630	3200	51.23	15.76	7.68	7.27	11.36	3.28	0.86	1.60	0.33	0.13	0.59	184	66.49	0.72	0.74
VAN7-88-03	−52.217	14.707	2984	49.93	16.49	7.49	6.91	11.25	3.32	1.07	1.70	0.25	0.15	0.63	141	65.94	0.68	0.87
VAN7-87-01	−52.235	14.789	3546	49.99	16.71	7.03	7.08	11.63	2.97	1.16	1.62	0.24	0.15	0.75	165	67.89	0.70	0.99
Orthogonal supersegment (15°45′–25°E)																		
VAN7-86-gl	−52.143	15.166	3738	49.13	15.67	10.22	8.82	10.33	3.33	0.02	1.82	0.14	0.18			64.43	0.66	0.02
KN162-9 64-01	−52.293	15.644	2950	49.87	15.95	9.93	7.81	10.68	3.10	0.14	1.91	0.18	0.17			62.27	0.67	0.10
VAN7-83-01	−52.173	15.837	3976	49.86	15.34	10.26	7.03	10.74	3.26	0.24	2.00	0.28	0.21	0.39	176	58.98	0.70	0.17
VAN7-80-04	−52.232	16.007	4038	50.21	15.88	9.08	7.55	10.78	3.01	0.33	1.85	0.16	0.21	0.40	170	63.56	0.68	0.25
VAN7-79-03	−52.296	16.125	4110	50.00	16.04	8.75	7.94	10.97	3.02	0.36	1.75	0.19	0.21			65.56	0.68	0.29
KN162-7 02-01	−52.330	16.233	4000	49.97	14.97	10.83	7.69	10.28	3.30	0.22	2.04	0.20	0.25	0.36	192	59.82	0.69	0.15

Table 3. (Continued)

Sample Number[a]	Latitude	Longitude	Depth	SiO_2	Al_2O_3	FeO*	MgO	CaO	Na_2O	K_2O	TiO_2	P_2O_5	MnO	H_2O	CO_2[b]	Mg#[c]	CaO/Al_2O_3	K/Ti
KN162-7 03-01	−52.299	16.507	3666	50.49	16.14	8.90	7.88	10.99	3.09	0.30	1.57	0.19	0.23			65.01	0.68	0.26
VAN7-78-01	−52.380	16.635	3901	48.91	16.23	10.50	7.55	10.59	3.11	0.16	1.69	0.24	0.22			60.13	0.65	0.13
AG22-01-01	−52.300	16.980	4000	49.83	16.37	8.98	8.65	11.53	2.89	0.10	1.49	0.16	0.14	0.18	256	66.89	0.70	0.09
KN162-7 04-13	−52.358	17.113	3650	49.83	15.82	9.47	8.00	10.86	3.16	0.23	1.74	0.21	0.20	0.35	201	63.94	0.69	0.18
KN162-7 05-01	−52.423	17.428	3030	50.50	14.95	10.78	6.61	10.42	3.38	0.41	2.11	0.26	0.23	0.46	178	56.25	0.70	0.27
KN162-7 06-02	−52.520	17.702	3586	49.73	16.19	9.62	7.92	11.01	3.15	0.22	1.64	0.17	0.21	0.31	166	63.31	0.68	0.19
KN162-7 07-02	−52.548	18.028	3913	50.12	15.31	10.04	7.93	10.27	3.22	0.25	2.00	0.23	0.16	0.37	247	62.35	0.67	0.17
AG22-03-01	−52.294	18.046	4200	49.62	15.54	9.93	8.14	10.44	3.22	0.13	1.84	0.15	0.19			63.25	0.67	0.10
KN162-7 08-05	−52.615	18.336	3713	49.84	15.74	9.72	7.54	10.69	3.28	0.23	1.93	0.22	0.16	0.39	177	61.93	0.68	0.17
KN162-7 09-01	−52.695	18.827	3932	49.69	15.98	9.09	8.34	10.94	3.07	0.16	1.64	0.18	0.15			65.81	0.68	0.13
AG22-05-01	−54.760	19.097	3700	49.31	16.86	8.95	8.29	11.02	3.15	0.12	1.47	0.13	0.15			66.03	0.65	0.11
KN162-7 11-02	−52.799	19.200	3913	49.24	15.93	9.97	8.90	10.50	3.17	0.13	1.63	0.14	0.19			65.17	0.66	0.11
KN162-7 10-21	−52.745	19.269	3097	49.60	16.13	9.09	8.04	10.83	3.17	0.23	1.73	0.20	0.20	0.33	189	64.97	0.67	0.18
VAN7-75-33	−52.995	19.775	1731	50.29	16.19	8.79	8.26	11.35	3.31	0.13	1.38	0.15	0.16			66.34	0.70	0.13
VAN7-74-01	−52.904	19.783	4130	50.27	15.18	9.95	7.42	11.11	3.22	0.10	1.80	0.14	0.18			60.99	0.73	0.08
KN162-7 13-29	−52.856	19.913	4067	50.08	15.57	9.47	7.96	10.87	3.27	0.18	1.72	0.17	0.19	0.29	213	63.81	0.70	0.15
KN162-7 15-05	−52.923	20.382	3403	49.84	16.31	8.68	8.20	11.19	3.11	0.20	1.45	0.18	0.19	0.30	170	66.46	0.69	0.19
KN162-7 14-01	−52.873	20.398	3403	49.59	16.24	9.12	8.05	10.98	3.16	0.14	1.62	0.15	0.19			64.93	0.68	0.12
KN162-7 16-01	−52.922	20.661	4235	50.14	15.63	9.08	8.08	11.61	3.00	0.10	1.58	0.17	0.22			65.12	0.74	0.09
VAN7-73-01	−52.976	20.693	3797	49.97	16.46	9.01	8.25	11.16	3.17	0.13	1.53	0.15	0.18			65.77	0.68	0.12
KN162-7 17-16	−52.949	20.925	3850	50.15	16.07	8.92	8.39	11.45	2.95	0.14	1.48	0.15	0.18	0.25	190	66.36	0.71	0.13
KN162-7 19-02	−53.050	21.376	3985	50.25	15.86	9.26	7.85	10.73	3.36	0.14	1.80	0.16	0.23			64.00	0.68	0.11
KN162-7 18-17	−52.990	21.406	4525	50.04	16.00	8.82	8.00	11.10	3.39	0.12	1.66	0.15	0.23	0.25	216	65.55	0.69	0.10
AG22-07-01	−53.023	21.833	3300	50.52	16.27	8.74	8.23	11.18	3.10	0.11	1.55	0.15	0.15			66.40	0.69	0.10
VAN7-70-87	−53.043	21.978	3869	50.08	16.20	8.85	8.41	10.94	3.23	0.12	1.57	0.14	0.18	0.23	196	66.59	0.68	0.11
KN162-7 20-01	−53.039	22.177	4170	50.09	16.70	8.03	8.62	11.09	3.14	0.13	1.39	0.14	0.18			69.23	0.66	0.13
VAN7-69-35	−53.135	22.451	3864	49.72	15.80	9.53	8.08	10.58	3.27	0.14	1.80	0.19	0.19			64.01	0.67	0.11
KN162-7 21-01	−53.035	22.468	3722	50.44	16.68	8.19	8.64	11.41	2.98	0.12	1.33	0.12	0.17			68.87	0.68	0.12
KN162-7 23-107	−53.173	22.547	3609	49.89	15.58	9.55	7.96	10.11	3.42	0.18	1.94	0.24	0.17			63.62	0.65	0.13
KN162-7 22-14	−53.109	22.647	3852	50.43	16.89	8.28	8.61	11.23	3.09	0.13	1.37	0.15	0.17	0.23	189	68.56	0.67	0.13
VAN7-68-01	−53.227	22.791	3323	50.46	14.80	10.00	7.34	11.26	3.20	0.14	1.74	0.15	0.20			60.63	0.76	0.11
KN162-7 24-03	−53.158	22.852	3202	50.36	16.65	8.31	8.72	11.42	3.01	0.10	1.37	0.14	0.18			68.76	0.69	0.10
AG22-09-01	−53.130	22.880	3800	50.27	16.61	8.07	8.61	11.72	2.94	0.06	1.29	0.14	0.11	0.18	182	69.10	0.71	0.06
VAN7-67-21	−53.285	23.019	3756	50.01	16.34	8.57	7.89	11.06	3.38	0.19	1.63	0.18	0.17			65.90	0.68	0.16
KN162-7 25-03	−53.173	23.117	3940	50.16	16.08	8.79	8.11	10.80	3.17	0.14	1.58	0.17	0.17	0.26	172	65.92	0.67	0.12
VAN7-66B-19	−53.277	23.271	3861	50.15	16.88	7.91	8.91	11.76	2.90	0.06	1.25	0.10	0.16			70.27	0.70	0.07
KN162-7 26-23	−53.214	23.358	3329	49.89	17.07	7.89	9.08	11.91	2.86	0.07	1.10	0.10	0.19	0.15	213	70.72	0.70	0.09
AG22 12-01	−53.393	23.692	3650	50.71	16.54	8.69	7.73	11.54	3.41	0.13	1.57		0.17			65.11	0.70	0.11
AG22 13-01	−53.408	24.758	3850	50.38	17.07	8.36	8.46	11.06	3.17	0.14	1.43		0.17	0.19	197	67.98	0.65	0.14

[a] Sample names are original and refer to the following cruises and publications: KN162-7 and KN162-9 are from back to back cruises aboard R/V *Knorr* in 2001 (unpublished). VAN7 is from 2003 cruise aboard the R/V *Melville* (unpublished). PS4 samples are from *Polar Stern* Leg ANT IV/4 [*le Roex et al.*, 1992]. AG22 samples are from 1981 *Agulhas* 22 expedition (largely unpublished).

[b] CO_2 abundance reported in ppm; analytical discussion in section 4.4 and auxiliary material.

[c] Mg# = 100 * $(Mg^{2+})/(Mg^{2+} + Fe^{2+})$; $Fe_2O_3/FeO = 0.15$.

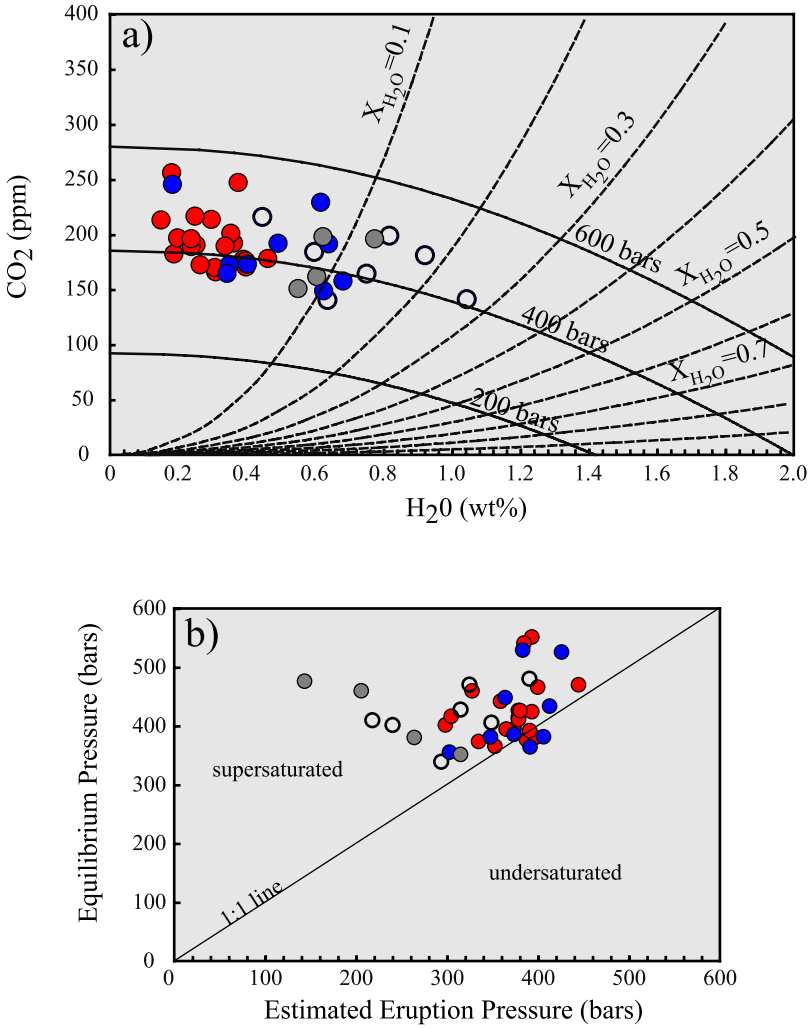

Figure 5. Dissolved water and carbon dioxide contents measured in SWIR glasses. (a) Vapor saturation diagram for tholeiites at 1200°C. Isobars (constant pressure) are shown as solid curves. Dashed curves are isopleths (constant vapor composition), marked with values of mole percent H_2O. (b) Equilibrium vapor saturation pressures plotted against dredge pressure. Dredge pressures are calculated from the depth at start of dredge and thus represent pressure maximums. The position of nearly all glasses above the 1:1 line indicates that they were supersaturated with a CO_2-rich vapor upon eruption, likely a result of rapid ascent rates that limit the amount of degassing before eruption.

ularity and dredge depths (Table 2b) to arrive at values reflecting the percent H_2O loss due to vesicle. The largest percentage H_2O loss by any sample (KN162-7-33-49) was 3.6% of the total measured H_2O concentration, which is less than the analytical error (4%) for the initial absorbance measurement. Therefore, we conclude that the amount of H_2O lost from any given sample is not significant.

3.4. Major Element Chemistry

[25] Three hundred fifty two fresh glasses were collected during the *Knorr* 162 (KN162 prefix) and *Melville* "Vancouver 07" (VAN7 prefix) cruises, along with 141 glasses from the 1986 R/V *Polar Stern* Ant IV-4 [*le Roex et al.*, 1992] and the 1981 SA *Agulhas*-22 expeditions. Samples were collected from 105 stations over 1050 km of ridge, resulting in a sampling frequency of 10 km. In an attempt to gain insight into the compositional variation of basalt erupted, station pairs along a single flow line were commonly picked to sample both zero-age basalt and presumably older, rift wall basalt. A higher proportion of the stations on the oblique supersegment are scattered across the rift valley and into the rift walls, corresponding to the disorganized volcanic morphol-

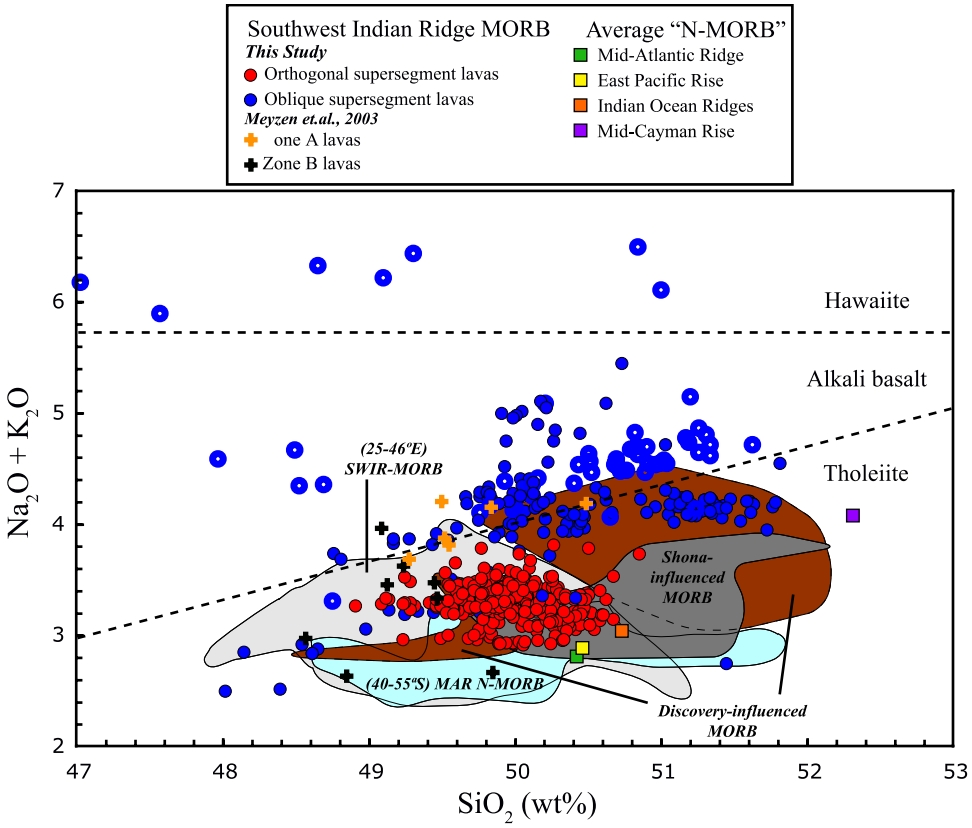

Figure 6. Basalt classification for SWIR lavas (9–25°E). Basalts are color coded by supersegment, with the orthogonal supersegment lavas (red circles) plotting separate from the oblique supersegment lavas (blue circles). Total alkalis ($Na_2O + K_2O$) versus SiO_2 classification plot [*Cox et al.*, 1979] including a dashed Hawaiian basalts divide [*Macdonald and Katsura*, 1964], which specifies alkali versus tholeiite basalt compositions. SWIR basalts are compared with average "normal" MORB compositions for the mid-Atlantic ridge (MAR, green square), East Pacific Rise (EPR, yellow square), and Indian Ocean (orange square) [*Su*, 2002], as well as Mid-Cayman Rise (MCR, purple square) [*Elthon et al.*, 1995]. Also plotted are fields representing neighboring ridge basalts from the southern MAR (40–55°S N-MORB, light blue; Shona-influenced MORB, dark gray; Discovery-influenced MORB, brown) [*le Roux et al.*, 2002c] and the central section of the SWIR (25–46°E) [*le Roex et al.*, 1989]. Orange and black pluses represent MORBs from farther east on the SWIR [*Meyzen et al.*, 2003].

ogy and absence of linear volcanic ridges, particularly within the amagmatic segments. Because of the large number of glass analyses we report representative major element compositions (Table 3) for an individual MORB glass from each dredge site (see Table S1 for complete data set). The 9–25°E basalts are divided into four groups corresponding to their tectonomagmatic province (described in section 2.2), and the basalts are plotted according to this grouping in all subsequent figures.

[26] Basalt compositions across the study area are quite variable, ranging from hypersthene-normative tholeiites to nepheline-normative alkali basalts. Overall, SiO_2 (47.5–51.8 wt %) is comparable to other southern ocean MORB suites, although total alkalis ($Na_2O + K_2O$) span a much broader range (Figure 6) covering much of the alkali olivine basalt field and extending into the hawaiite compositional field (>5.75 wt % total alkalis). Orthogonal supersegment basalts plot exclusively in the tholeiite field (Figure 6), with an average composition systematically lower in silica and higher in alkalis than average N-MORB from the EPR, MAR, and IO (Table 4) [*le Roux et al.*, 2002a; *Su*, 2002], but similar to other parts of the SWIR [*le Roex et al.*, 1989]. They also overlap slightly with SWIR Zone B lavas from 52 to 61°E (black pluses) [*Meyzen et al.*, 2003]. The majority of lavas from the oblique supersegment, however, are transitional to alkalic, similar to the SWIR Zone A lavas

Table 4. Average Basalt Composition for Each Tectonomagmatic Province, Compared With Average MORB Compositions[a]

	Orthogonal Supersegment	SD	Amagmatic Accretionary Segments[b]	SD	Joseph Mayes Seamount	SD	Narrowgate Segment	SD	9–25°E "Normal" MORB[c]	SD	Global "Normal" MORB	SD	MAR "Normal" MORB	SD	EPR "Normal" MORB	SD	Indian Ridges "Normal" MORB	SD	Mid-Cayman Rise MORB[d]	SD
SiO_2	49.98	0.32	50.54 (49.67)	0.84 (0.81)	50.14	0.21	50.28	1.06	49.96	0.47	50.48	0.54	50.42	0.46	50.46	0.49	50.73	0.5	52.31	0.34
Al_2O_3	16.19	0.52	16.71 (17.34)	0.50 (0.60)	15.22	0.33	16.28	0.43	16.56	0.73	15.43	0.69	15.50	0.54	15.05	0.60	15.93	0.8	15.69	0.5
FeO*	9.00	0.64	8.15 (8.32)	0.69 (0.54)	10.18	0.89	7.96	0.79	8.62	0.67	9.98	0.95	10.03	0.85	10.51	0.70	9.18	0.9	9.55	0.69
MgO	8.21	0.49	7.67 (8.28)	0.55 (0.83)	6.00	0.85	6.56	0.81	8.44	0.55	8.05	0.60	8.24	0.51	7.73	0.56	8.22	0.6	6.53	0.64
CaO	11.06	0.36	10.61 (10.86)	0.46 (0.52)	10.26	1.06	10.94	1.00	11.37	0.40	11.55	0.58	11.44	0.54	11.62	0.40	11.37	0.7	9.8	0.46
Na_2O	3.16	0.15	3.52 (3.65)	0.37 (0.55)	3.79	0.36	3.47	0.41	3.13	0.36	2.77	0.35	2.71	0.34	2.77	0.20	2.91	0.5	3.78	0.21
K_2O	0.16	0.07	0.46 (0.12)	0.13 (0.06)	0.67	0.19	1.28	0.33	0.09	0.02	0.12	0.07	0.10	0.04	0.12	0.06	0.13	0.1	0.3	0.06
TiO_2	1.59	0.21	1.57 (1.35)	0.21 (0.30)	2.11	0.35	1.80	0.24	1.42	0.25	1.49	0.27	1.42	0.21	1.64	0.27	1.42	0.3	1.98	0.28
P_2O_5	0.15	0.06	0.25 (0.15)	0.06 (0.06)	0.36	0.09	0.39	0.09	0.13	0.05	0.15	0.05	0.14	0.04	0.16	0.06	0.14	0.1	0.3	0.07
H_2O	0.29	0.09	0.54 (0.26)	0.13 (0.11)	0.63	0.10	0.74	0.20	0.17	0.02	-	-	-	-	-	-	-	-	-	-
Mg#[e]	64.3	2.8	65.1 (66.3)	2.9 (2.3)	53.6	5.6	61.8	5.5	65.9	2.8	59.0	-	59.4	-	56.7	-	61.5	-	54.9	-
K/Ti	0.1	0.1	0.40 (0.12)	0.10 (0.04)	0.4	0.1	1.0	0.2	0.1	0.0	0.12	-	0.10	-	0.10	-	0.13	-	0.21	-
Fractionation corrected[f]																				
Na_8	3.18	0.14	3.42 (3.67)	0.34 (0.44)	3.22	0.14	3.05	0.30	3.16	0.21	2.74	0.3	2.74	0.3	2.63	0.2	2.96	0.4	3.24[g]	0.05
Fe_8	9.09	0.46	7.78 (8.27)	0.64 (0.68)	8.21	0.27	6.78	0.38	8.72	0.50	9.78	0.8	10.04	0.7	9.91	0.6	9.22	0.9	7.13[g]	0.17
Si_8	50.89	1.50	50.50 (49.78)	0.81 (0.63)	49.83	0.22	50.06	1.10	-		-	-	-	-	-	-	-	-	-	-
Ti_8	1.62	0.13	1.42 (1.35)	0.12 (0.22)	1.28	0.05	1.20	0.12	-		-	-	-	-	-	-	-	-	-	-
K_8	0.16	0.06	0.42 (0.13)	0.11 (0.04)	0.46	0.12	0.94	0.19	-		-	-	-	-	-	-	-	-	-	-
H_2O_8	0.29	0.1	0.48 (0.26)	0.11 (0.06)	0.44	0.1	0.54	0.1	0.20	0.04	-	-	-	-	-	-	-	-	-	-
K_8/Ti_8[h]	0.14	0.05	0.41 (0.13)	0.12 (0.04)	0.50	0.12	1.11	0.31	0.06	0.02	0.07	-	0.06	-	0.06	-	0.08	-	0.13	-

[a] Averages of "normal" MORB are taken from *Su* [2002].
[b] Average values for low-K/Ti lavas are in parentheses.
[c] 9–25°E N-MORB is derived by averaging all lavas from this study with K/Ti $\leq$ 0.09.
[d] Mid-Cayman Rise MORB values are averages of *Elthon et al.* [1995] (see Table 2).
[e] Mg# = 100 * (Mg/(Mg + Fe^{2+})), where Fe^{2+} is FeO*.
[f] See text and auxiliary material for details of element-8 corrections.
[g] Na_8 and Fe_8 values for Mid-Cayman Rise MORB taken from *Meyzen et al.* [2003].
[h] Values for global oceans are not fractionation corrected.

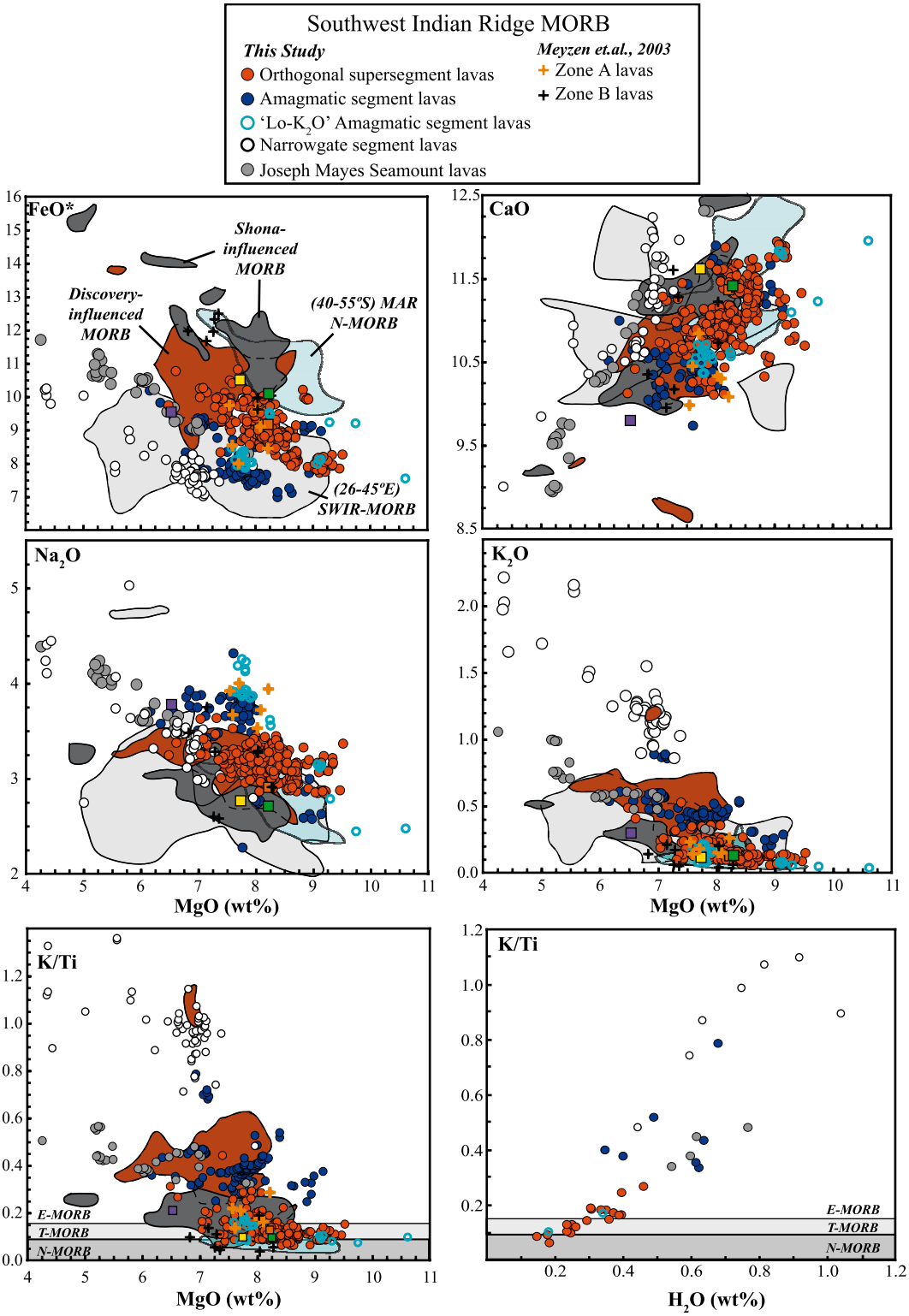

Figure 7. Representative major element compositional space showing SWIR basalts divided into tectonomagmatic provinces; orthogonal supersegment (solid red circles), amagmatic segment lavas (solid dark blue circles), low-k/Ti amagmatic segment lavas (open light blue circles), Joseph Mayes Seamount lavas (solid gray circles), and the Narrowgate segment lavas (open black circles). Also plotted are nearby MORB suites as in Figure 6. "Normal" MORB average compositions as in Figure 6. Horizontal gray fields in K/Ti panels are based on the following limits: N-MORB has K/Ti < 0.09, T-MORB has K/Ti from 0.09 to 0.15, and E-MORB has K/Ti > 0.15 and K_2O > 0.2 wt % [*Cushman et al.*, 2004; *Langmuir et al.*, 1992; *Schilling et al.*, 1983; *Sinton et al.*, 1991].

(Figure 6) from the obliquely spreading eastern SWIR (61 to 70°E) [*Meyzen et al.*, 2003]. The average alkali contents of the oblique supersegment lavas are similar the ultraslow spreading Mid-Cayman Rise basalts [*Thompson et al.*, 1980], which are believed to be the products of very low degrees of mantle melting resulting in abnormally thin ocean crust [e.g., *Dick et al.*, 1984; *Klein and Langmuir*, 1987].

3.4.1. Orthogonal Supersegment

[27] The orthogonal supersegment lavas span a large range in MgO (6.48–9.52 wt % MgO), with higher FeO* (7.73–10.83 wt %) and TiO_2 (1.05–2.16) and lower Al_2O_3 (14.49–17.96 wt %) at a given MgO than our other tectonomagmatic provinces (Figure 7). The only exception is TiO_2 and FeO* in a few amagmatic segment basalts. Along-axis profiles (Figure 8) show generally smooth east to west gradients of increasing FeO* and H_2O, and decreasing Al_2O_3, CaO (not pictured), and Mg# (69.5–53.7). The progressive drop in Mg# is negatively correlated with estimated crustal thickness (Figure 4), suggesting increased differentiation with thickening crust toward the west. Na_2O and SiO_2, uncorrected for fractionation, show little variation along the length of the orthogonal supersegment.

[28] On the basis of the classification of *Cushman et al.* [2004], lavas from 25 to 19°E are dominantly N-MORB and T-MORB, with K/Ti values between 0.06 and 0.44, while T-MORB and E-MORB are more abundant from 19 to 16°E. The most depleted basalts (lowest K/Ti) occur on the eastern end of the supersegment with a relatively constant K/Ti of ~0.1 from 25 to 21°E. From 21 to 16°E the range and average K/Ti progressively increase (Figure 8). Orthogonal supersegment lavas are clearly separated in K/Ti and K_2O from our other three geographic groups (Figure 7), with the exception of the low-K/Ti amagmatic segment lavas (<0.2 K/Ti), which will be discussed in detail below.

3.4.2. Oblique Supersegment

[29] The oblique supersegment lavas as a group display much greater compositional variation than the orthogonal supersegment lavas. Basalt compositions within each oblique supersegment province vary markedly (Figure 8) and correlate with the changing ridge morphology. Below we discuss the details of each tectonomagmatic province within the oblique supersegment.

3.4.2.1. Amagmatic Accretionary Segments

[30] The amagmatic segment basalts display the greatest intraprovince compositional variation of the four groups (Figure 8), especially for SiO_2, Na_2O, and TiO_2 (not shown). Amagmatic segment lavas mostly have higher Al_2O_3 and Na_2O, and lower FeO* and TiO_2 at a given MgO, relative to the orthogonal supersegment lavas, but similar FeO* and Al_2O_3 to Narrowgate segment basalts and Na_2O and K_2O to Joseph Mayes Seamount basalts (Figures 8 and 9). Their most distinctive feature is the bimodal nature of K/Ti and K_2O. As a result, we have denoted a "low-K/Ti" group of amagmatic segment basalts with K/Ti < 0.20 and K_2O < 0.22 wt.% that overlap with the orthogonal supersegment lavas. The rest of the amagmatic segment basalts have K/Ti > 0.2, similar to Joseph Mayes Seamount lavas, with four samples as high as Narrowgate segment basalts (Figures 7 and 8). Curiously, the low-K/Ti amagmatic segment lavas (N-MORB) are not distinctive from the rest of the group for most other major element oxides, particularly the E-MORB with which they are most closely associated geographically. There is a clear inverse correlation between MgO and Na_2O defining the upper limit for most of our remaining data that indicates high initial sodium contents in the parental melts, and may reflect low-degree melts of the depleted host peridotite.

3.4.2.2. Joseph Mayes Seamount

[31] Basalts from Joseph Mayes Seamount are distinct in their overall high extent of differentiation and well correlated inter element variations with Mg# from 64.2 to 40.7. As a result, they are the most tightly constrained compositional group (e.g., SiO_2, Al_2O_3, and H_2O; Figure 7), and form well-defined linear trends on oxide versus MgO plots (Figure 9). They are not as enriched as the Narrowgate segment lavas, but have higher average K/Ti, H_2O, and Na_2O than the orthogonal supersegment basalts. FeO* abundances are highest for Joseph Mayes Seamount lavas, but extend down to overlap the amagmatic segment lavas (Figure 8). Al_2O_3 and CaO are consistently lower than the other provinces at a given MgO (except for some overlap with the Narrowgate segment), which likely reflects the influence of low-pressure crystallization involving Cpx.

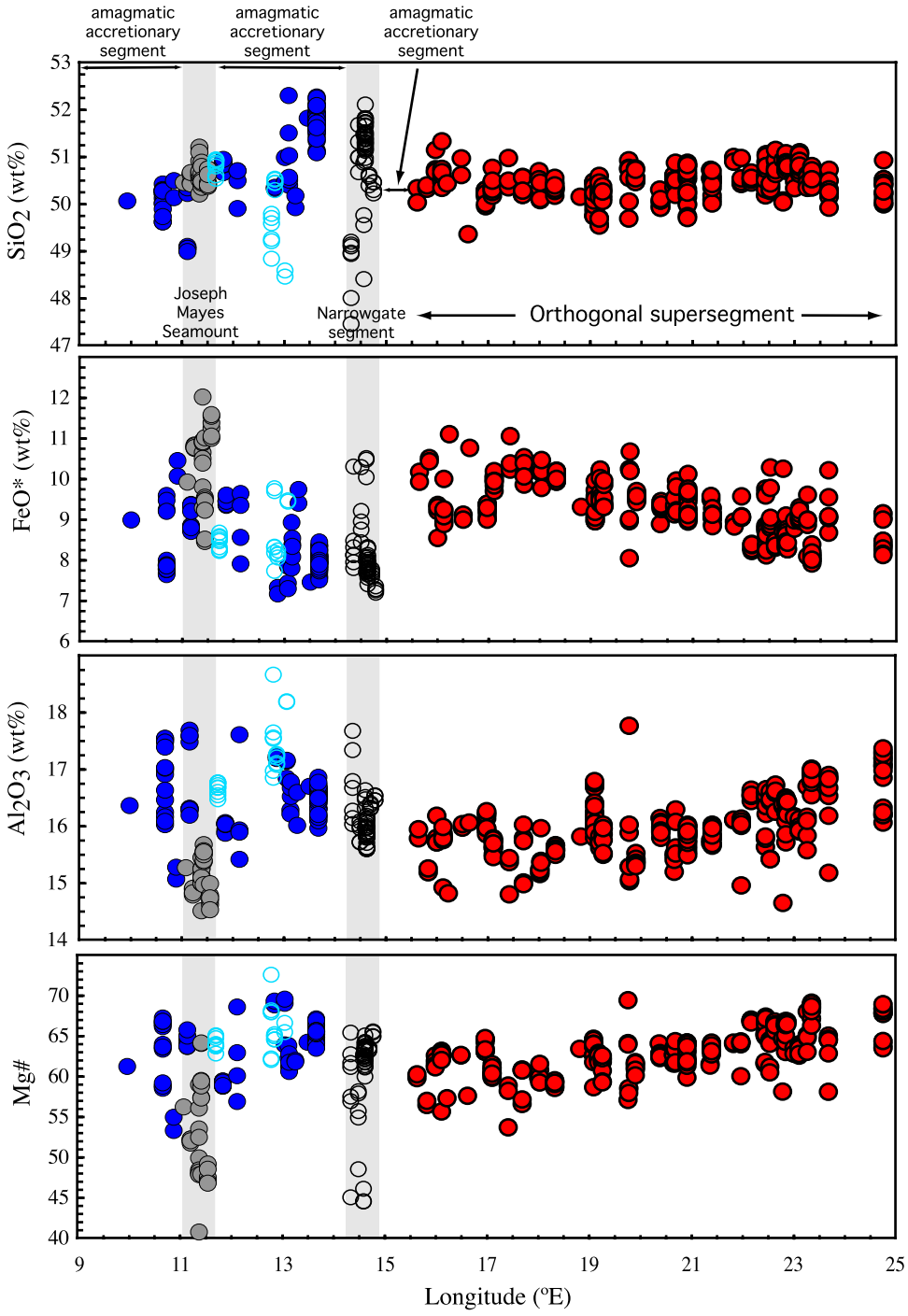

Figure 8. Along-axis basalt major element compositional variations. Symbols for each tectonomagmatic province are the same as in Figure 7. Light gray vertical fields designate Joseph Mayes Seamount and Narrowgate segment provinces. Fields for K/Ti are the same as in Figure 7. Mg# = 100 * $Mg^{2+}/(Mg^{2+} + Fe^{2+})$, where $Fe_2O_3/FeO^* = 0.15$.

3.4.2.3. Narrowgate Segment

[32] Narrowgate segment lavas have Mg#s as low as 44.5. The basalts generally display a limited range in most oxides, with the exception of a few lavas, although SiO_2 does have the largest range of any tectonomagmatic group. Although FeO* for the entire group is low relative to the rest of the

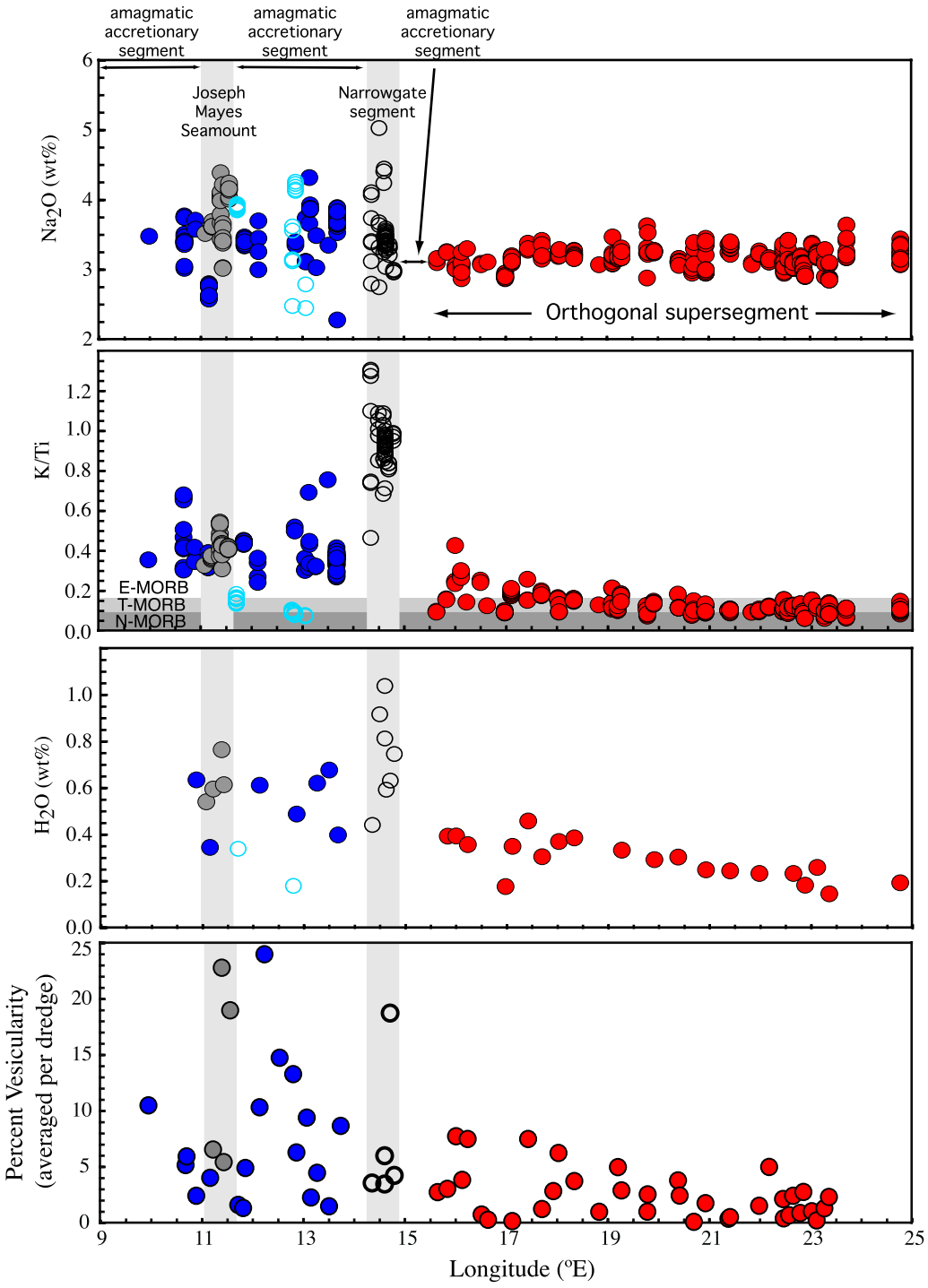

Figure 8. (continued)

basalts, most Narrowgate segment lavas are fairly primitive (Figure 8). TiO_2, CaO and Na_2O are most similar to Joseph Mayes Seamount lavas. By far their most distinctive aspect is their elevated K/Ti (0.48–1.36) and H_2O (0.44–1.04 wt %), which are higher than for any other basalt group. With such elevated water contents it is likely that low FeO* contents are related to hydrous fractionation (see below) and the associated suppression of plagioclase

saturation. This may also account for the elevated Al_2O_3 contents in a number of evolved lavas.

4. Petrogenetic Results

4.1. Major Element Differentiation

[33] Trends of decreasing MgO with increasing FeO*, Na_2O, K_2O, and TiO_2, and decreasing Al_2O_3 and CaO, indicate fractional crystallization of olivine, plagioclase, and clinopyroxene. Clearly though, the breadth in major element oxide compositions for the entire suite (e.g., the difference in FeO* between the two supersegments) cannot be explained by fractional crystallization of a single parental melt over a range of pressures (Figure 9). Model liquid lines of descent (LLD) generated using "hBasalt" [*Weaver and Langmuir*, 1990] (v.6; originally called "BASALT," see [*Langmuir et al.*, 2006]) fit the observed data much better when appropriate regional parent compositions and a range of pressures are used. At higher pressure the phase field of clinopyroxene expands at the expense of olivine and plagioclase [e.g., *Bender et al.*, 1978; *Grove et al.*, 1992; *Kushiro*, 1964; *Schilling et al.*, 1983], and clinopyroxene appears on the liquidus at higher MgO contents. In Figure 9 (e.g., CaO) the pressure dependence of Cpx saturation is illustrated by the orthogonal supersegment LLDs (thick red curve is 0.9 GPa with Cpx saturation at >8 wt % MgO versus thin red curve for 0.1 GPa with Cpx saturating at 7 wt % MgO), suggesting that most of the orthogonal supersegment lavas could have experienced high-pressure fractional crystallization. While polybaric fractional crystallization can explain much of the compositional variation within the orthogonal supersegment, it cannot account for much of the variation between the oblique supersegment provinces.

[34] Each of the four oblique supersegment basalt groups (including the low-K group) has distinctive major element characteristics requiring diverse parental melts. At constant MgO, glasses from the amagmatic segments have the highest Na_2O, Al_2O_3, and SiO_2, and lowest CaO, possibly requiring a different parental magma produced by low degrees of melting. The low-K amagmatic glasses have even higher Na_2O, which when coupled with distinctly lower K_2O and K/Ti, suggests parental magmas produced by very low degrees of melting of a more depleted source than other oblique supersegment basalts. Joseph Mayes Seamount glasses are similar to the amagmatic glasses except they have lower SiO_2 and Na_2O and slightly higher CaO for a given MgO. Narrowgate segment and Joseph Mayes Seamount basalt Na_2O, TiO_2, and CaO variations are similarly fit by 10–50% low-pressure fractional crystallization (Figure 9). Although some additional scatter (especially SiO_2 and Al_2O_3) could be attributed to melt rock reaction during late-stage transport through the shallow mantle or lower crust [*Lissenberg and Dick*, 2008], the Narrowgate segment lavas plot at distinctly lower FeO* and higher K_2O and K/Ti, requiring a unique parental melt. Using an amagmatic segment parental melt with 0.74 wt % H_2O (average measured Narrowgate segment content; dashed blue line in Figure 9) we modestly fit much of the Narrowgate segment suite (except K_2O and K/Ti), as elevated H_2O in basaltic melt suppresses plagioclase saturation relative to clinopyroxene and olivine saturation [*Kushiro*, 1972, 1975; *Michael and Chase*, 1987; *Yoder and Tilley*, 1962]. Low and variable FeO* contents along with the elevated CaO and Al_2O_3 are also commonly seen in other E-MORB suites where H_2O is high [e.g., *Asimow et al.*, 2004; *Christie et al.*, 2005; *Cushman et al.*, 2004].

[35] Finally, LLDs show only ~0.02 change in K/Ti over the plotted range of MgO, thereby accounting for little variation in K_2O and K/Ti. This observation highlights the inability of fractional crystallization to explain many of the compositional differences both between and within the tectonomagmatic units. It also reinforces our conclusion that various parental melt compositions, derived from variable degrees of melting and/or heterogeneous source material, are necessary to explain the entire suite.

Figure 9. Major element oxide compositional variation versus MgO. Symbols as in Figure 7. LLDs modeled using "hBasalt" for representative parental compositions from each supersegment (red, orthogonal supersegment; blue, oblique supersegment). Thin LLDs = 0.1 GPa and thick LLDs = 0.9 GPa. Thin dashed blue line represents LLD for amagmatic parental composition with 0.74 wt % water (average Narrowgate lava concentration). TiO_2, K_2O and K/Ti panels only show low-pressure LLDs, as LLD has little sensitivity to pressure. Grey dashed line in CaO panel reflects Cpx saturation filter. This filter calibrates MORB data from specific ridges according to experimentally determined L + Ol + Plag + Cpx, L + Ol + Plag, and L + Ol cotectics, allowing quantification of a lower limit of CaO associated with the Ol + Plag cotectic (see *Herzberg* [2004, Figure 4] for details).

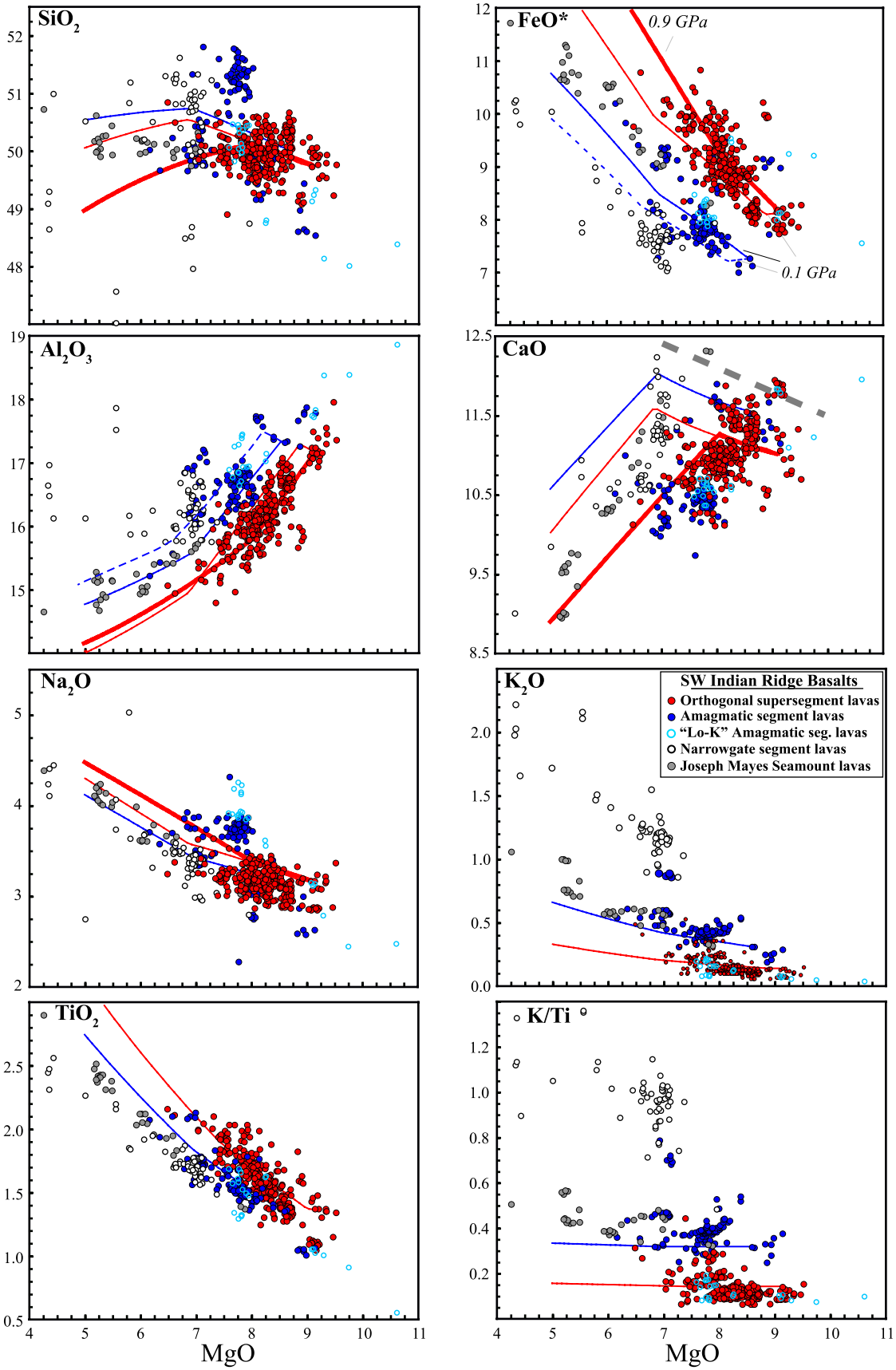
SiO2
FeO*
0.9 GPa
0.1 GPa
Al2O3
CaO
Na2O
K2O
SW Indian Ridge Basalts
Orthogonal supersegment lavas
Amagmatic segment lavas
"Lo-K" Amagmatic seg. lavas
Narrowgate segment lavas
Joseph Mayes Seamount lavas
TiO2
K/Ti
MgO
MgO

Figure 9

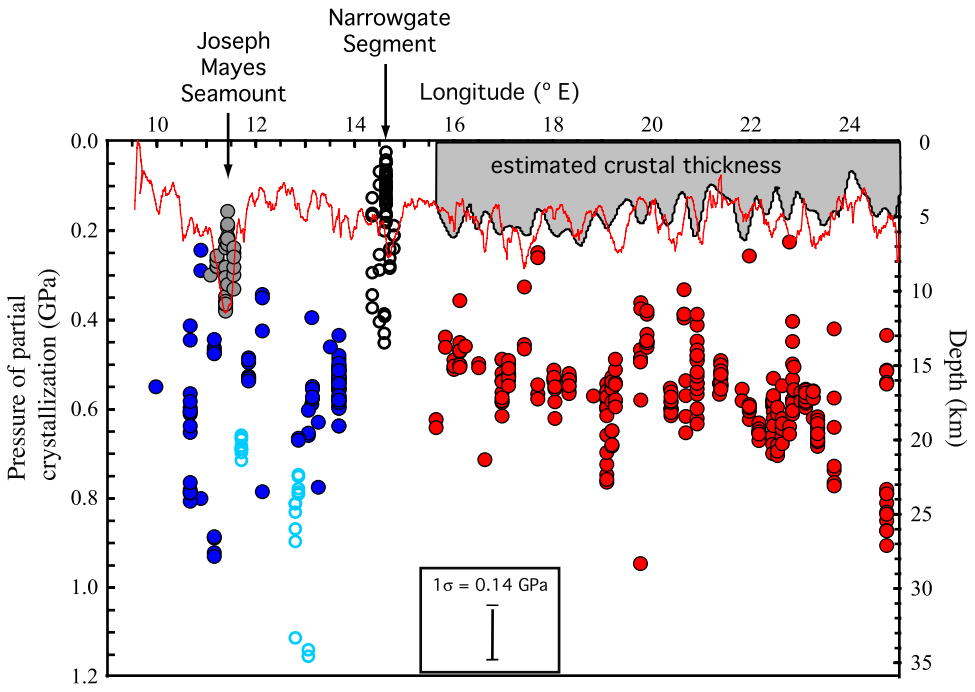

Figure 10. Pressures of partial crystallization calculated assuming three-phase saturation (Ol + Cpx + Plag), using the method of *Herzberg* [2004]. Estimated crustal thickness field (gray) and bathymetrically compensated crustal thickness (thin red curve) profiles from Figure 4.

4.2. Partial Crystallization Pressure

[36] Here we calculate partial crystallization pressures (the theoretical depth of initial Cpx-Ol-Pl saturation) using the method of *Herzberg* [2004], which is based on experimental data for the cosaturation of clinopyroxene, plagioclase, and olivine [e.g., *Grove et al.*, 1992; *Herzberg*, 2004; *Michael and Cornell*, 1998; *Tormey et al.*, 1987]. Assuming that these pressures preserve information of early crystallization history, they may reflect the transition from increasing melt mass to decreasing melt mass and thus provide an estimate for the cessation of mantle melting (i.e., base of the lithosphere). *Michael and Cornell* [1998] and *Herzberg* [2004] showed that regional variations in the pressure of partial crystallization correlated with spreading rate. However, neither study included data from an ultraslow spreading ridge.

[37] This calculation is only applicable to lavas that have crystallized Cpx, thus we use various methods to independently confirm Cpx crystallization (e.g., correlation between CaO and Sc, petrographic observation, etc.) and also apply the CaO versus MgO filter used by *Herzberg* [2004] (see Figure 9 caption for details). The vast majority of 9–25°E basalts fall below this cotectic limit and are thus considered to have been in equilibrium with L + Ol + Plag + Cpx during a portion of their lithospheric evolution. There are also various other caveats and pitfalls that could potentially influence the interpretation of these calculated pressures of partial crystallization, and the most pertinent and important are discussed in the auxiliary material (Text S1).

[38] Estimated partial crystallization pressures for the 9–25°E basalts span a large range from 1 atm to just below 1.2 GPa (Figure 10). Despite the variability, the bulk of the calculated pressures (0.2–0.8 GPa) are similar to lavas from the Mid-Atlantic Ridge [*Herzberg*, 2004; *Michael and Cornell*, 1998]. Lavas from the orthogonal supersegment give pressures from 0.2 to 0.8 GPa, with a clear gradient in dredge-averaged pressures from 0.7 GPa at 25°E to 0.4 GPa near 16°E. This correlates with increasing crustal thickness and decreasing average Mg#, and is consistent with increased lithospheric cooling approaching 25°E due to the Du Toit fracture zone [*Grindlay et al.*, 1998]. Partial crystallization pressures for the individual tectonomagmatic units within the oblique supersegment also vary dramatically (from 1 atm to 1.1 GPa) and are consistent with the variable ESRs. Amagmatic segment basalts extend from 0.2 to 1.1 GPa, covering most of this range, with the low-K lavas (light blue circles) plotting at pressures >0.6

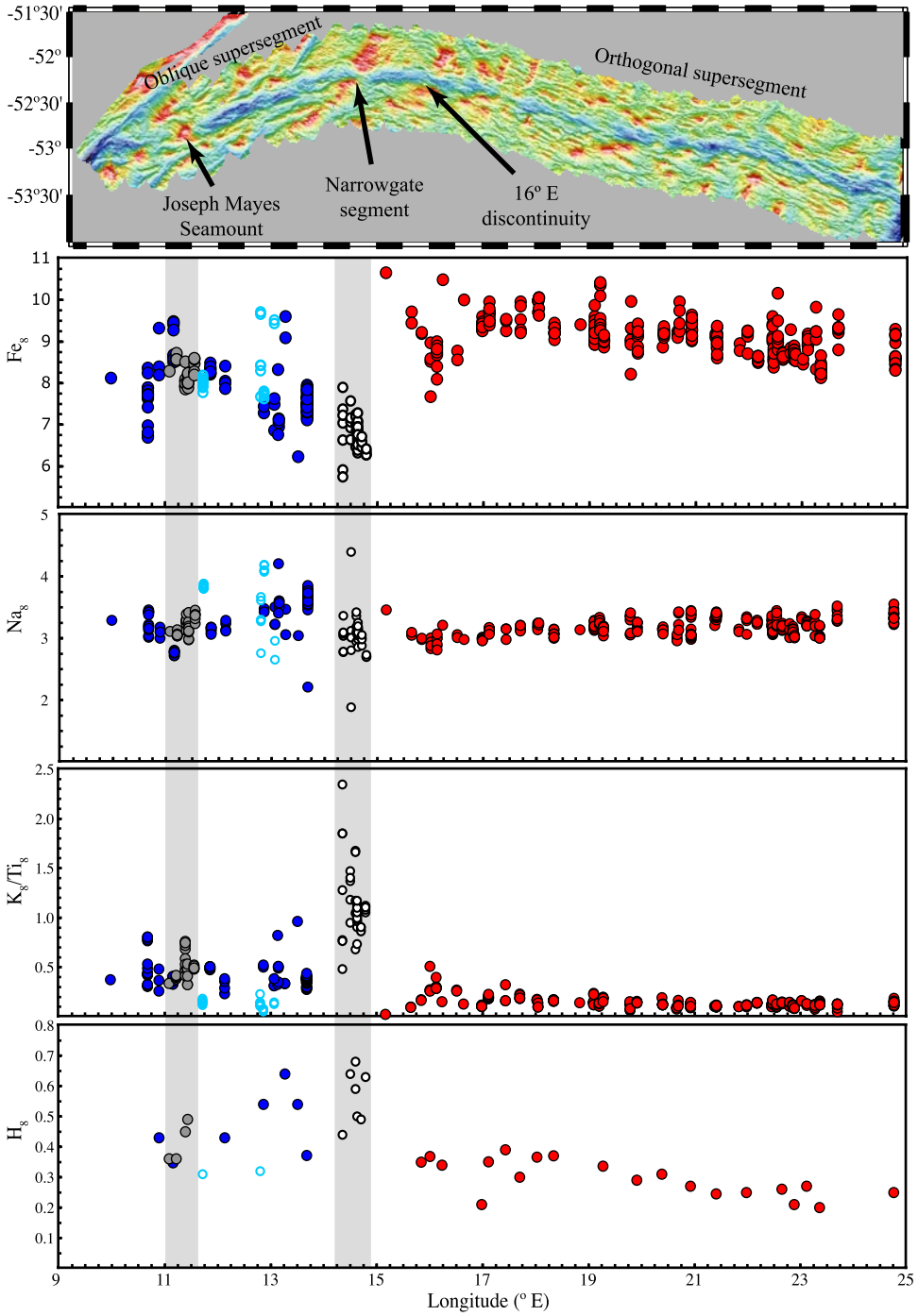

Figure 11. Fractionation-corrected glass compositions from 9 to 25°E. Symbols and fields are the same as in Figure 7. Fractionation correction is described in the auxiliary material (Table S1) and Table 5.

GPa. Such variability is not surprising considering the changing lithospheric thickness, and the resulting effect on melting and late-stage fractionation within a cooler than normal lithosphere. Both the Narrowgate segment and Joseph Mayes Seamount lavas plot at significantly lower pressures than either the amagmatic segment or orthogonal supersegment lavas, even though their spreading rates are similar to the latter. Many EPR basalts also plot at similarly low pressures, yet the inferred upwelling rates for Narrowgate and Joseph Mayes Seamount segments are only 14.2 and 13.3 mm/a, respectively.

Table 5. Regression Slopes for LLD Trends for Each Tectonomagmatic Province[a]

Tectonomagmatic Province (Basalt Group)	SiO_2	FeO*	Na_2O	TiO_2	K_2O	H_2O
Olivine + plagioclase + clinopyroxene multisaturated						
Joseph Mayes Seamount	−0.158	−0.982	−0.288	−0.414	−0.105	-
Narrowgate cross-axis high	−0.158	−0.825	−0.288	−0.414	−0.235	-
Amagmatic segment	−0.158	−0.982	−0.288	−0.414	−0.105	−0.127
Orthogonal supersegment	−0.069	−1.097	−0.288	−0.474	−0.051	−0.047
Olivine + plagioclase saturated						
Joseph Mayes Seamount	−0.408	−0.751	−0.202	−0.273	−0.050	-
Narrowgate cross-axis high	−0.408	−0.644	−0.202	−0.273	−0.050	-
Amagmatic segment	−0.408	−0.751	−0.202	−0.273	−0.050	-
Orthogonal supersegment	−0.382	−0.952	−0.202	−0.302	−0.051	-
Olivine saturated						
Joseph Mayes Seamount	−0.246	0.121	−0.083	−0.048	−0.032	-
Narrowgate cross-axis high	−0.246	0.121	−0.083	−0.048	−0.032	-
Amagmatic segment	−0.246	0.121	−0.083	−0.048	−0.032	-
Orthogonal supersegment	−0.246	0.121	−0.083	−0.048	−0.032	-

[a] All slopes are linear regressions of LLDs fit to basalt data. In element-specific cases where LLDs for multiple provinces are the same or where statistical significance (R^2) is low, a single slope is used. Only glasses with MgO > 4.5 wt % are corrected. Glasses with <8 wt % MgO are corrected using olivine + plagioclase + clinopyroxene multiphase saturation slopes. Glasses with 8.0 < MgO < 8.5 are corrected using the olivine + plagioclase saturation slopes. All glasses with >8.5 wt % MgO are first corrected to 8.5 wt % MgO using the respective olivine only saturation slope, and then corrected to 8 wt % MgO using the olivine + plagioclase saturation slope. Because of the small number of H_2O analyses, regressing samples from individual provinces is not statistically meaningful, thus we use the regressed slope for the entire LLD, assuming ol + pl + cpx saturation across the entire range of MgO, for each supersegment.

[39] It is possible, as noted by *Lissenberg and Dick* [2008], that interaction between MORB melt and primitive lower oceanic crustal cumulates could cause a shift toward lower CaO and higher Al_2O_3 and MgO melt compositions due to formation of high-Mg# pyroxene. These authors point out that melt rock reaction is most likely to occur at slower spreading rates where initial undercooling of intrusions likely creates a semirigid crystal mush creating high permeability in the cumulate pile required for this to proceed. While melt-rock reaction may mask or emulate the effects of high-pressure fractionation, as of yet there exist no quantitative methods of discriminating the relative chemical importance of melt-rock reaction versus high-pressure fractionation during evolution of MORB melts. Regardless, the observed relationship between spreading rate and calculated initial partial crystallization pressure does imply a first-order connection between basalt chemistry and tectonics.

4.3. Parental Melt Variation (Along-Axis)

[40] Along-axis profiles of fractionation corrected oxide values illustrate substantial differences in both absolute value and chemical systematics between the two supersegments (Figure 11 and Table 5). Fe_8 on the orthogonal supersegment increases slightly from east to west with the majority of the lavas having higher values than lavas on the oblique supersegment (with the exception of several amagmatic segment lavas). In contrast to Fe_8, the orthogonal supersegment lavas Na_8 show a small but systematic decrease from east to west, consistent with the evidence for greater melt production and thicker crust to the west.

[41] The basalts from 16–25°E on the SWIR cluster near the high Na_8/low Fe_8 end of the global array of *Klein and Langmuir* [1987] (Figure 12), while those from the oblique supersegment mostly lie above it at even higher Na_8/lower Fe_8. The

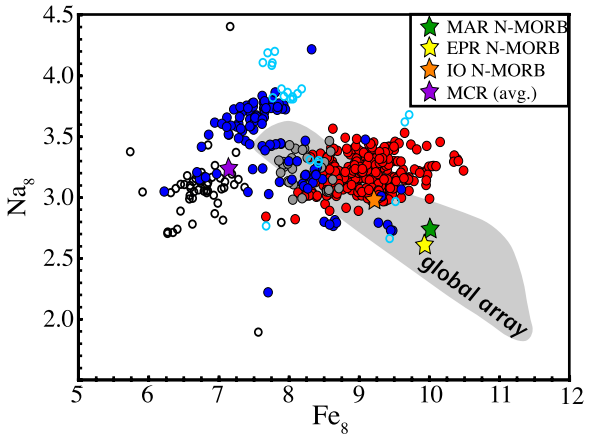

Figure 12. Na_8 versus Fe_8 for 9–25° SW Indian Ridge basalts plotted with "global array" [*Klein and Langmuir*, 1987]. N-MORB data for MAR, EPR, and Indian Ocean taken from *Su* [2002], and Mid-Cayman Rise data taken from *Elthon et al.* [1995] and *Meyzen et al.* [2003].

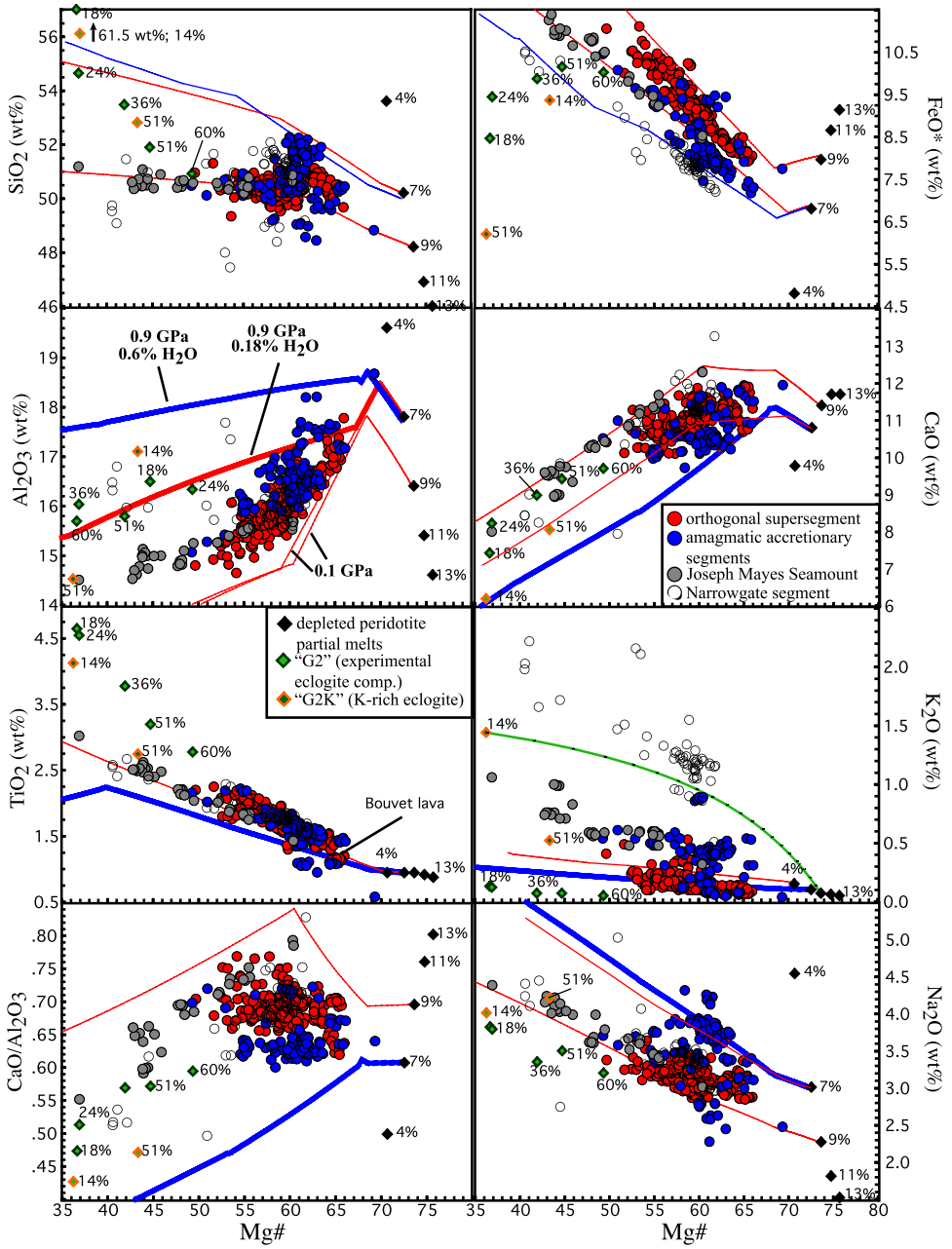

Figure 13. SWIR major element basalt compositions plotted with published experimental melt compositions. Black diamonds represent modeled near-fractional aggregate melts of a depleted spinel lherzolite [*Kinzler*, 1997]. Green and orange diamonds are experimental partial melts of the "G2" and K-rich "G2K" eclogite/pyroxenite compositions from *Pertermann and Hirschmann* [2003]. Data symbols for lavas as in Figure 7 and details of model LLDs as in Figure 9. The green curve reflects a binary mixing curve between a 9% peridotite melt and 14% K-rich pyroxenite melt, with 5% mixing increments and assuming equal densities. Mg# = 100 * Mg/(Mg + Fe), where all Fe is FeO*.

Meyzen et al. [2003] zone A lavas at the eastern end of the SWIR similarly cluster above Na_8 of 3.5 and $Fe_8 \sim 8.0$. Conventionally, this implies colder mantle that started melting at shallower depth, resulting in low mean melting pressure and low extents of melting However, one would expect higher Fe_8 in zone A and our study area due to the thicker lithospheric cap (Figure 12). Moreover, over half our data lie outside the global array and notably do not fit the global trend at the superseg-ment scale, defining orthogonal trends to it. *Niu and Batiza* [1993] propose that such trends locally indicate highly variable melt-rock reaction during melt transport through the mantle, which would be

consistent with the expected thicker lithospheric lid along the SWIR than at faster spreading ridges. Indeed, ultraslow spreading ridges are generally deeper with colder and thicker lithosphere, thus implying both lower degree melts and greater transport distances through the conductive layer where melt-rock reaction is likely extensive.

[42] The limited, but systematic, Na_8 variation along axis (except for a few elevated Na_8 amagmatic segment lavas) helps constrain the origin of the more highly variable Fe_8, K_8/Ti_8, and H_8. Forward fractionated variable degree, polybaric fractional melts (Figure 13; black diamonds) [*Kinzler*, 1997] of a depleted spinel lherzolite (derived by 1% melting of primitive upper mantle [*Hart and Zindler*, 1986]) illustrate that a 7–9% aggregate melt can explain the bulk of the Na_2O data (and much of the other oxide data), but can only account for K_2O on the orthogonal supersegment. The elevated K_2O of the oblique supersegment lavas, especially the Narrowgate segment lavas, would require unrealistically low degrees of melting (<1%), which is contrary to the Na_8 signal. The variations in K_8/Ti_8 and H_8, then, most likely represent preferential melting of an enriched source heterogeneity in the mantle, as signaled by the large K_8/Ti_8 offset between the orthogonal supersegment and the Narrowgate segment lavas (Figure 11).

[43] K_8/Ti_8 and H_8 in the orthogonal supersegment lavas also systematically increase from east to west, likely then corresponding to a gradual enrichment in mantle source heterogeneities, even while the degree of mantle melting inferred from Na_8 increases (as commonly seen along ridges toward enriched hot spot sources). Further west, the K_8/Ti_8 and H_8 of the oblique supersegment are statistically higher than all but the westernmost orthogonal supersegment lavas, implying an even more enriched source beneath the oblique supersegment. They also correlate well with other indicators of an enriched source, including long-lived isotopic compositions ($^{143}Nd/^{144}Nd$, $^{87}Sr/^{86}Sr$, $^{208}Pb/^{204}Pb$, $^{176}Hf/^{177}Hf$) [*le Roex et al.*, 1992; *Standish*, 2005] and critical trace element ratios (e.g., La/Sm).

5. Discussion

[44] Mid-ocean ridge basalt, though the most homogenous of all terrestrial lavas [e.g., *A. E. J. Engel et al.*, 1965; *C. G. Engel*, 1965], is still compositionally heterogeneous at virtually all scales from ocean basin to individual dredge, even when corrected for crystal fractionation. MORB suites can rarely be attributed to a single parent magma, requiring the generation of multiple parent melts in the source region. At the SWIR from 9 to 25°E we find usual and often extreme heterogeneity on the supersegment (~1000 km), intrasegment (~50 km), and dredge (<0.5 km) scales. These local and regional variations must be explained by any model proposed for the composition of the local source mantle, and the processes by which magmas are derived from it. It must also account for the apparent dynamic relationships we observe between basalt chemistry, ridge geometry, and geology.

[45] Many previous models [e.g., *Dick et al.*, 1984; *Klein and Langmuir*, 1987] account for variations in MORB major element composition via melting of a homogeneous upper mantle: commonly depleted garnet/spinel lherzolite. We immediately rule out, however, the possibility of a homogeneous depleted peridotite as the source for our MORB suite on the basis of the fivefold range and along-axis variations of K_8 and K_8/Ti_8, together with previously documented correlations between basalt incompatible element ratios and isotopic composition [*le Roex et al.*, 1992; *Standish*, 2005]. These observations, as noted above, plus documented local residual mantle neodymium isotopic heterogeneity [*Salters and Dick*, 2002; *Warren*, 2007] require the presence of a heterogeneous source mantle consisting of both a depleted and an enriched component at local, segment, and supersegment scales. Before addressing the influence of ridge geometry and ESR on basalt chemistry from 9 to 25°E, we first address the nature of the enriched component below.

5.1. Melting Anomalies and the Character of the 9–25°E MORB Source

[46] It is clear from the local- and segment-scale distribution of E-MORB (i.e., K/Ti variability) that enriched lithologies are large enough to allow generation and extraction of a significant volume of melt. As a result the associated enriched isotopic and trace element signature is preserved during aggregation and transport through the mantle. We therefore deduce that small widely dispersed populations of enriched veins would have little influence on the erupted basalt compositions; as exchange with the mantle during melt aggregation and transport to the crust would almost certainly eliminate any enriched signature.

[47] A second constraint on the mantle source is the systematic major (e.g., K_2O) and trace element [*Standish et al.*, 2004] compositional gradient from 16 to 25°E (Figure 11) that accompanies relatively uniform melt production and higher and virtually constant ESR. While this argues for a systematic westward increase in the population of mantle heterogeneities, the length scale of the heterogeneities must be much shorter than the average segment length (10–35 km; see page 5). This is required for the melt aggregation and transport processes to effectively average out most, but not all, of the source variability at the local to segment scale. On the basis of the above constraints together with recent observations within abyssal peridotites from the same area [*Shimizu et al.*, 2006a; *Warren et al.*, 2006] that the length scale of veining is ~1 km, while the length scale of melt-rock reaction is closer to ~1 cm, we estimate the length scale of individual heterogeneities to be <1 km.

[48] The dramatic changes in magma chemistry and melt production west of 16°E on the oblique supersegment would seem at first most easily explained by abrupt discontinuities in mantle composition, with the geochemical anomalies at Narrowgate and Joseph Mayes Seamount requiring a local enriched fixed mantle source. While Joseph Mayes Seamount has existed for only ~1 Ma, and thus could reflect melting of such a source, the trace of the Narrowgate magmatic segment extends out past 8 Ma rift mountain crust. This trace and that seen at the 16°E discontinuity both define V-shaped trends indicating plate-driven eastward migration at 13 and 16 mm/a respectively. This motion is opposite the direction of the Bouvet Hotspot track, therefore, these are melting anomalies and cannot be the product of fixed heterogeneities in the underlying asthenosphere.

[49] We interpret the extreme major element variability found between 9 to 16°E to reflect the changing ridge geometry, and subsequent variable extents of melting and melt-rock reaction; the latter two involving a mantle source similar to that beneath 16 to 25°E. However, K_8-Ti_8 and H_8 trends (Figure 11) suggest that the proportion of enriched heterogeneities in the underlying mantle continues to systematically increase west of 16°E, with growing proximity to the ancient Bouvet Hotspot trace. While to a first order, ridge basalt chemistry at fast and slow spreading ridges is largely governed by the composition of the mantle source, at ultraslow spreading ridges with highly variable ESR, the potential exists for the first-order chemical variability to be more a function of the melt generation process itself. However, we note that *Cannat et al.* [2008] suggest the basalt chemical variability on the eastern end of the SWIR, where spreading geometry is less variable, to be dominantly controlled by the mantle source.

5.2. Nature and Origin of the Enriched Component

[50] The needed heterogeneities in the 9 to 25°E mantle source region could reflect local trace element enrichment in a fairly uniform major element composition mantle, or alternatively could be accompanied by a significant contrast in major element composition. Many possibilities for the latter exist (e.g., incorporation of recycled sediment or crust, metasomatic veining of the mantle), but only in this case does the presence of multiple solidi lead to bimodal melting behavior. This difference is critical to explaining the abrupt changes in geochemistry along the SWIR. In particular, the changes in MORB chemistry from 9 to 16°E, can be readily accounted for by an enriched low-volume component with a more basaltic composition that melts at higher pressure than the depleted host mantle. In this case, the large K_8/Ti_8 and H_8 anomalies at the Narrowgate segment represent accumulated deep low-degree melts of the enriched component, where melting of the host mantle may be inhibited or play a lesser role in the erupted lava compositions. It is difficult to see how this could occur in a mantle with a more uniform major element composition where the solidus temperature of enriched and depleted mantle would be similar.

[51] We observe the major element compositions of E-MORBs from Joseph Mayes Seamount, Narrowgate segment, and the amagmatic segments to be similar to Bouvet Hotspot lavas (avg. Na_2O = 3.6, K_2O = 1.3, SiO_2 = 48.6) [*Weaver*, 1991]. This is not surprising as *le Roex et al.* [1992] previously documented many geochemical affinities between a subset of basalts from ~12–15°E and the Bouvet Hotspot basalts. They interpreted this compositional similarity to indicate that upwelling of enriched Bouvet plume material produced low-degree melts that refertilized the surrounding ambient mantle, which then generated the E-MORB. The data presented here bolster their general model, however our greater along-axis coverage and density of sampling together with well constrained locations for the Bouvet plume from 15 to 30 Ma indicate the influence of this refertilized mantle to be farther

reaching than just 12–15°E. This is illustrated by the systematic westward enrichment along the orthogonal supersegment (section 4.3).

[52] It is also possible that the SWIR from 9 to 25°E is part of a South Atlantic mantle province contaminated by advection of upper mantle material from beneath the lithospheric roots of the Archaean African craton [*Meyzen et al.*, 2007]. They propose that the seismically determined southerly upper mantle flow field emanating from beneath the African craton [*Behn et al.*, 2004] may produce localized upwellings within the South Atlantic mantle due to the viscous drag exerted by the continental keel [*Meyzen et al.*, 2007]. The Bouvet Hotspot, then, would be the product of one such upwelling. Presumably melts generated during earlier Bouvet upwelling would be preferentially tapping the enriched component derived from the subcontinental asthenosphere, as proposed for the South Atlantic near the Shona and Discovery Hotspots [*le Roux et al.*, 2002b]. That the Bouvet plume may originate as a localized upwelling from beneath the African craton does not preclude present-day E-MORB generation along the SWIR via melting of an enriched, previously refertilized, mantle source.

5.3. Mafic Lithologies in the SWIR MORB Source

[53] The importance of mafic lithologies as a second source component in MORB and OIB generation has garnered a great deal of attention lately [e.g., *Donnelly et al.*, 2004; *Ito and Mahoney*, 2004a; *le Roux et al.*, 2002b]. Direct evidence of their existence in the convecting asthenosphere is difficult to attain, yet their presence is often inferred from MORB geochemistry [e.g., *Hirschmann and Stolper*, 1996; *Hirschmann et al.*, 2003; *Kogiso et al.*, 2004; *Sun and Hanson*, 1975; *Zindler et al.*, 1984], ocean island basalt [e.g., *Ito and Mahoney*, 2004a; *Weaver*, 1991], and near-axis seamount basalt generation [*Niu and Batiza*, 1997]. Although primary mafic lithologies (veins) have yet to be documented in the upper mantle beneath the SWIR, a number of rather persuasive lines of evidence strongly suggest the presence of an enriched mafic lithology beneath 9–25°E.

[54] Abyssal peridotites, commonly interpreted as the residues of mantle melting beneath ocean ridges [e.g., *Dick et al.*, 1984; *Johnson et al.*, 1990; *Michael and Bonatti*, 1985], were often collected in the same dredge haul as our basalts and consist of veined (pyroxenite or gabbro) and unveined harzburgites and lherzolites [*Warren et al.*, 2006; *Warren*, 2007]. Detailed analyses of Cpx grains from host peridotites and pyroxenite veins indicate subdredge-scale homogeneity in major and trace elements, versus considerable variability among dredges. Yet, significant isotopic variability (equal or greater than the basalt range) does exist both within dredges and between them and this heterogeneity is attributed to melt-rock reaction [*Warren*, 2007], particularly for those peridotites from 9 to 16°E possessing abundant mafic veining. Additionally it was recognized that these peridotites extended to higher Nd isotopic values than the spatially associated basalts, requiring a missing isotopically enriched lithology [*Salters and Dick*, 2002] whose low melting temperature relative to depleted upper mantle explains its absence in mantle emplaced to the base of the crust. While the observed small-scale chemical variation may not require a missing "vein component" in the strict sense of the term, it is consistent with prior metasomatism of the host asthenosphere by Bouvet material [*Shimizu et al.*, 2006b; *Warren et al.*, 2006], and is consistent with measured basalt compositions [*le Roex et al.*, 1992; *Standish et al.*, 2004]. Independent evidence from basalt Hf isotopic compositions and trace element fractionation further supports the presence of an enriched mafic or pyroxenitic component beneath 13–15°E on the SWIR [*Janney et al.*, 2005].

5.4. Melting of Mafic "Pyroxenite" Lithology and Peridotite

[55] Natural pyroxenites cover a wide range of major element compositions, but eclogites commonly have higher alkalis and Al_2O_3 at lower Mg# than pyroxenites from xenoliths and massifs [*Hirschmann and Stolper*, 1996], and therefore may be a more appropriate model source component for explaining the alkali-rich Narrowgate segment lavas. This is important, as to our thinking the latter would most closely reflect the nature of the mantle heterogeneities from 9 to 16°E. Experimental studies by *Pertermann and Hirschmann* [2003] show their "G2" eclogitic pyroxenite solidus at 2 and 3 GPa to be 190 ± 25°C and 170 ± 25°C cooler than the anhydrous depleted peridotite solidus [e.g., *Hirschmann*, 2000; *Walter*, 1998; *Yaxley and Green*, 1998], thus mantle melting would actually commence during upwelling when the lower-temperature mafic lithology solidus is reached. This type of bimodal melting of an enriched mafic lithology at high pressure plus

low-pressure partial melting of ambient depleted peridotite is the foundation of our melting model.

[56] To illustrate some of the compositional similarities between experimental melts of mafic lithologies and E-MORBs from this study we plotted "G2" and "G2K" (Figure 13), where "G2K" indicates a K_2O-rich renormalized oxide concentration relative to "G2" [*Pertermann and Hirschmann*, 2003]. FeO*, Al_2O_3, and Na_2O are similar between the "G2/G2K" melts and typical Narrowgate segment lavas, however SiO_2 and TiO_2 are noticeably higher and CaO slightly lower in the former. Of particular significance is the similarity in K_2O between the 14% "G2K" melt and the Narrowgate segment lavas, as well as the 51% "G2K" melt and the Joseph Mayes Seamount lavas. To estimate potential compositions derived by mixing of enriched melts of a mafic lithology with 9% melts of depleted lherzolite, we calculated a simple binary mixing curve (green line), assuming equal densities for the end-member melts. Although this mixing curve does not fit the most elevated K_2O concentrations of the Narrowgate segment lavas, it does suggest an explanation for some of the basalts.

[57] The importance of bimodal melting becomes more evident when we apply the *Pertermann and Hirschmann* [2003] model specifically to Narrowgate segment. In this light, the 7 km of crust at Narrowgate segment would be produced by partial melting of passively upwelling refertilized mantle with ~5% eclogitic pyroxenite, plus partial melting of depleted peridotite between 50 and 10 km depth [see *Pertermann and Hirschmann*, 2003, Figure 7]. Since the difference between the onset of pyroxenite versus peridotite melting controls their relative contributions to the aggregate melt [*Hirschmann and Stolper*, 1996], a mantle source beneath Narrowgate segment having 5% pyroxenite is interpreted to indicate that 40% of the erupted lava at Narrowgate was derived from pyroxenite melting [*Pertermann and Hirschmann*, 2003].

5.5. Mafic Melt Extraction

[58] Field observations of ophiolitic dunites reveal relationships between pyroxenite veins, replacive dunites, and host peridotite that shows mafic (vein) melting incorporates a limited volume of the surrounding peridotite [*Dick*, 1977]. Upwelling asthenosphere triggers vein melting and the consumption of heat, yet to maintain thermal equilibrium, heat must flow from the enclosing depleted mantle to the melting region, thereby permitting vein melting to continue, but at the same time inhibiting melting in the nearby peridotite because of the loss of heat and subsequent departure from the adiabat. Spatially associated abyssal peridotites collected along with the 9–25°E basalts include depleted harzburgite, lherzolite, and dunite, some with pyroxenite veins with textural and chemical characteristics suggestive of variable degrees of melting and/or melt-rock reaction [*Warren*, 2007]. Modal analysis found 2–13% Cpx, again suggesting variable F, with depleted to enriched trace element compositions, in line with the large basalt range.

[59] The local range in basalt major element compositions thus may reflect primary melt signatures of the source or result from melt-mantle reaction. As *Reiners* [1998] points out, there are two dominant end-member mineralogical reactions that occur during melt-mantle interaction: (1) $Melt_1$ + Lherzolite $\Rightarrow$ $Melt_2$ + Olivine or (2) $Melt_1$ + Lherzolite $\Rightarrow$ $Melt_2$ + Pyroxenite. While both reactions are well documented in mantle peridotites [e.g., *Kelemen and Dick*, 1995; *Sen*, 1988], and both dunite and pyroxenite are present in the 9–26°E peridotites, dunite volumetrically far outweighs pyroxenite. Here we interpret the abundance of dunite versus pyroxenite and their size variability as an indicator of their importance for melt extraction over a large range of scales [*Braun and Kelemen*, 2002; *Kelemen et al.*, 2000].

5.6. Mantle Melting Column as a Reactive Transport Filter

[60] While it is difficult to assess the relative importance of melt-mantle interaction on MORB chemistry, we suggest the large range in modal Cpx and associated variable depletion of the mantle column is critical. The modal mineralogy of the mantle column largely determines its buffering capacity and impact on the incompatible element budget of melts passing through it. Melt movement through an upwelling mantle matrix whether in dunite channels or through harzburgite or lherzolite occurs by reactive transport. As a result, the reactive capacity of the mantle through which a given melt is flowing can play an important role in determining how closely the erupted melt resembles the incipient melt. *Reiners* [1998] and *Dick* [1989] recognized that the reactive capacity of mantle, through which successive batches of melt flow, will decrease because of the increasing chemical equilibrium attained within the mantle by ongoing mineralogical reactions. Both diffusive

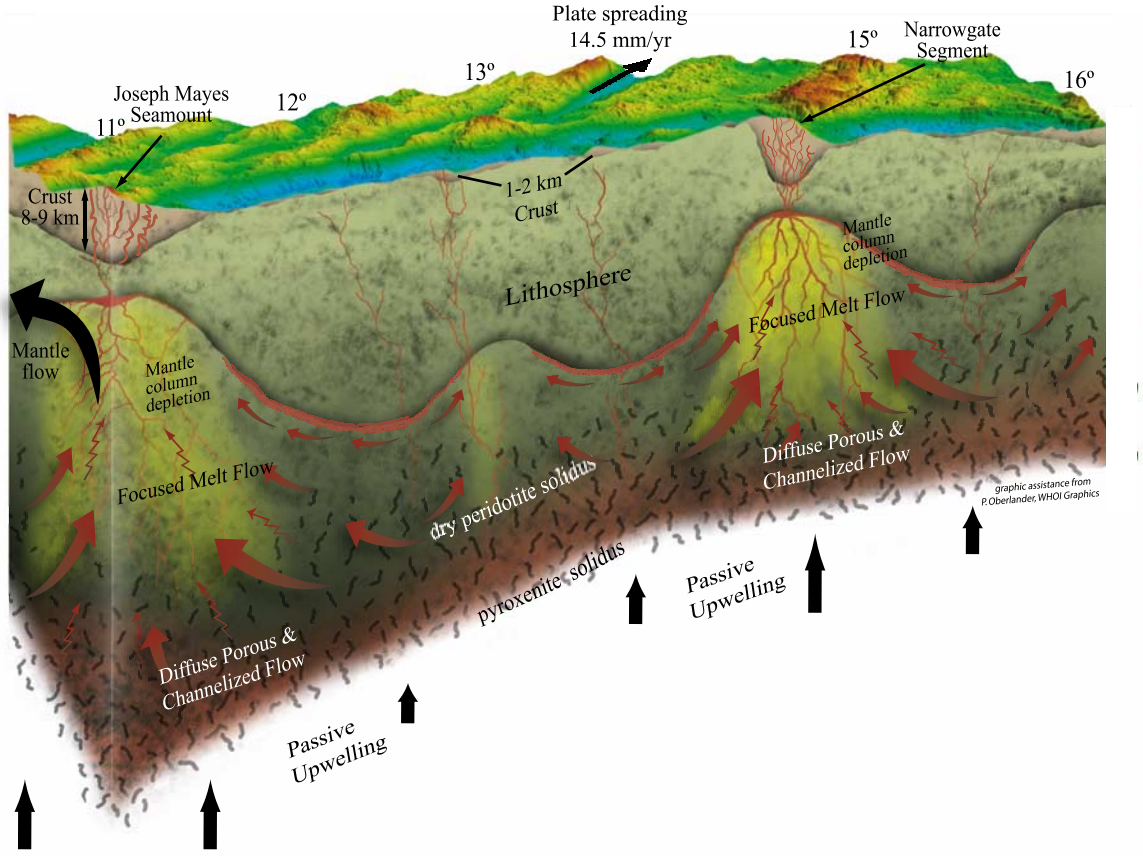

Figure 14. Schematic 3-D along-axis cross section illustrating our tectonomagmatic MORB generation model for the oblique supersegment on the SWIR (9–16°E). Top surface is seabeam bathymetry (map view in Figure 1) covering a ~300 km long portion of the ridge (~11 to 16°E). At the base of the image, depleted mantle containing >5% mafic veins (black pattern) passively upwells at various inferred rates ranging from 14 mm/a (large arrows) to 7 mm/a (small arrows). Melting initiates at the solidus of the mafic lithology, which can be much deeper than the anhydrous peridotite solidus. Extraction and focusing of deep mafic melts can occur via both diffuse porous flow (small irregular red arrows) and channelized flow via dunite conduits (large solid red arrows), both of which presumably involve some melt-mantle reaction. Variable mantle depletion resulting from the total volume of melt produced and thus transported through each mantle column is represented by the yellow shading beneath JMS and the Narrowgate segment, where the latter is more depleted (brighter yellow). This makes sense, as Narrowgate segment has been magmatically robust for at least 8 Ma, while JMS is constrained to be younger than 1.2 Ma. Thus, the mantle column beneath the Narrowgate segment is more depleted, with less Cpx and therefore a lower TE buffering capacity relative to JMS. Lithospheric thickness varies along axis as a function of spreading geometry (i.e., conductive cooling). Resulting variable lithospheric thicknesses may have two important effects: (1) thick lithosphere would limit the length of the melting column (i.e., thinner crust) and (2) variable lithospheric thickness could influence along-axis melt focusing. The thin black arrow parallel to and extending from the extinct transform trace at 14°E indicates the spreading direction and full spreading rate. Thick curved black arrow represents mantle flow.

exchange and replacement of Cpx by Ol will equally result in melt compositions arriving at the top of the column that will trend (over time) toward the isotopic and trace element composition of the original incipient melt.

[61] On the basis of the nearly constant ESR (i.e., lithospheric thickness), melt production along the orthogonal supersegment should be relatively constant from segment to segment, resulting in similarly depleted mantle with essentially steady state reactive capacity. On the oblique supersegment, however, the evolving ridge geometry, lithospheric thickness, and segment age all suggest that the reactive capacity of the mantle column beneath each segment is different (Figure 14).

[62] If we assume that the proportion of pyroxenite in the source is similar beneath Joseph Mayes Seamount and the Narrowgate segment, and their

respective melting columns are the same height, then the difference in major and trace element compositions, particularly the K_2O and K/Ti enrichment, could largely be attributed to the difference in age of each magmatic segment; Joseph Mayes Seamount, on the basis of spreading ages, is 1.8 Ma old and Narrowgate is 11.5+ Ma old. Gravity, magnetics, seafloor morphology, and peridotite sampled along the lithospheric flow line (including a piston cored serpentinite at 52°31.9′S, 11°37.0′E; see Figure 3a) show that the Joseph Mayes portion of the ridge was largely amagmatic over the previous 8+ Ma. Thus, the underlying mantle column would have processed little melt prior to the present magmatic event beginning 1.8 Ma. As a result, the mantle column beneath the Joseph Mayes segment would not have been stripped of clinopyroxene and associated incompatible elements to the same degree as that beneath Narrowgate segment. Accordingly, the trace element buffering capacity of the Joseph Mayes Seamount mantle column is likely much greater than for the Narrowgate segment, where volcanism was continuous over the last 11.5+ Ma. If the same enriched melt composition is produced near the base of both mantle columns, the higher trace element buffering capacity of the mantle beneath Joseph Mayes Seamount could then account for its parental melts, which are less enriched in incompatible elements (i.e., lower K/Ti) than the Narrowgate segment lavas. This might also account for some aspects of other major element differences as well (e.g., Figure 9), though we do not attempt to resolve this issue here.

[63] One of the major anomalies in our data set is the unexpected presence of significant N-MORB in close spatial proximity to E-MORB within the amagmatic segments. Unexpected because the low ESRs would imply thickened lithosphere and decreased melting, as indicated by the thin to missing crust, which is not generally associated with N-MORB production. So, the intuitive prediction, based on the predominance of deep, low-degree partial melts of a refertilized mantle source, would be for E-MORB compositions. We put forth two possible reasons for the surprising amount of N-MORB within the amagmatic segments. First, the mantle beneath these amagmatic segments will have undergone relatively low degrees of melting, thus retaining high percentages of Cpx (2–13% modal Cpx). With such a high incompatible element buffering capacity, and a very small volume of melt migrating through it, continued melt-rock reaction between enriched, deep initial melts and a relatively fertile ambient mantle could produce N-MORB-like compositions. Second, smaller overall melt volumes compared to more robust segments diminishes the opportunity for locally derived partial melts from different depths within the melting column to mix. Hence, it is more likely that an individual batch of magma might directly reflect the composition of the local source that in a heterogeneous mantle could be either enriched or depleted.

[64] On the other hand, where melt transport volumes are large and the mantle columns are successively reacted and stripped of Cpx (e.g., Narrowgate segment and the orthogonal supersegment), melts retain their initial trace and incompatible element characteristics. Additionally, robust magmatic segments would promote mixing, thereby tending to average out the influence of small-scale heterogeneities. Thus, at faster spreading rates, with a relatively uniform process, magmas tend to more directly reflect the composition of the bulk mantle source region. In contrast, where steady state melting and melt transport does not exist, stochastic variations in local melt transport volumes, small-scale mantle heterogeneities, and prior mantle melting history can result in large local variations in the extent of mantle-melt reaction and MORB chemistry.

5.7. Length and Top of the Mantle Melting Column

[65] The amount and composition of melt produced beneath a ridge is largely a function of the total length of the mantle-melting column. While the bottom of the column is a function of the initial mantle temperature, the top is specifically the depth where melt mass begins to decrease rather than increase with continued upwelling. Although melting begins at different depths for pyroxenite and peridotite, because of the rapid depletion of the vein component, cessation of melting likely occurs at one depth. The top of the melting column is a function of mantle upwelling rate, which controls the influence of conductive cooling. While theoretically small at faster rates, the influence of conductive cooling is likely large at ultraslow spreading rates, where modeling crustal thickness produced by partial melting of anhydrous peridotite shows it drops off precipitously below 20 mm/a [*Bown and White*, 1994; *Reid and Jackson*, 1981; *White et al.*, 2001].

[66] Not only does thickened lithosphere beneath the amagmatic segments decrease the total amount

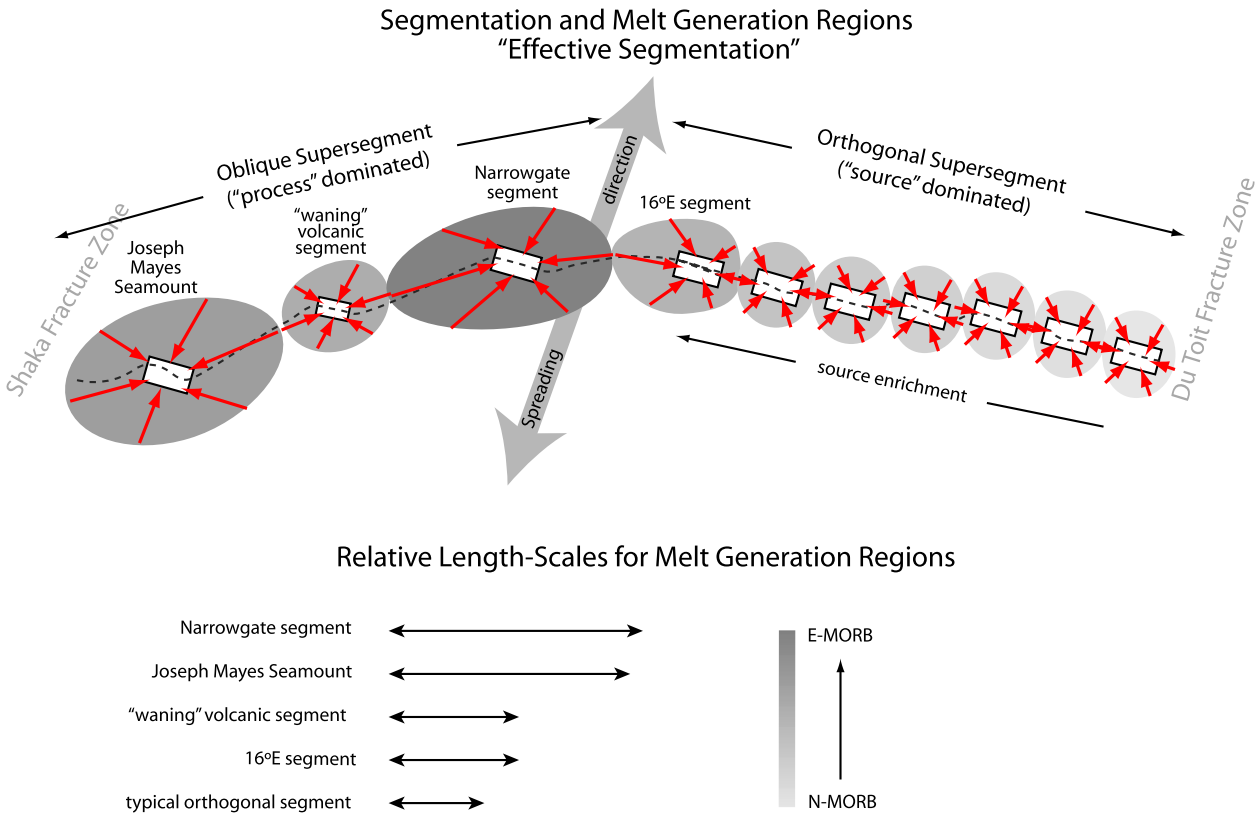

Figure 15. Schematic illustration (map view) of 9–25°E magmatic segmentation and associated "effective segmentation" (see text for definition). Red arrows indicate simplified direction of melt focusing beneath each magmatic segment, based on modeled flow lines [*Barry et al.*, 2005; *Montesi et al.*, 2006] and theoretical slope of lithospheric base. Variably shaded gray ovals represent the "effective segmentation" for each magmatic segment derived from segment spacing and along-axis lithospheric topography. The shade of gray reflects the relative enrichment of lavas for each segment and is a function of the mantle source, but more so the "effective segmentation." Dashed line is the ridge axis.

of melting and crustal thickness, but it also substantially increases the relative proportion of deep, enriched mafic-derived melt to depleted peridotite melt in the melting zone. We believe this plays a major role in determining the composition of the Narrowgate segment and Joseph Mayes Seamount basalts. *Ito and Mahoney* [2004a] similarly noticed that the aggregate melt composition generated beneath segments experiencing increased conductive cooling were significantly more sensitive to changes in the relative proportion of pyroxenite.

5.8. Along-Axis Melt Focusing and "Effective Segmentation"

[67] The makeup of aggregate melts from a given melting regime likely reflects its shape [e.g., *O'Hara*, 1985], therefore the area over which melt is produced for a respective segment is important to consider as well as the depth to the top of the melting column at any one point. MORB enrichment has previously been attributed to across-axis focusing of low-degree melts from the "wings" of a 2-D triangular melting regime [*Galer and O'Nions*, 1986], yet along-axis focusing of even more low-degree enriched melt volumes [*Plank and Langmuir*, 1992] could further augment the enriched melt signal. We investigate this possibility by proposing a model that calls upon segment-scale variations in lithospheric thickness to help explain both the variations in crustal thickness and MORB chemistry.

[68] On the basis of variable ESRs and the influence of conductive cooling, theoretical models [*Bown and White*, 1994] suggest thickened lithosphere and decreased melt production beneath oblique amagmatic segments. Decreased melt production stems from the depression of the top of the melting column, which means melts produced

beneath the amagmatic segments will be derived from melting of a more enriched bulk source (i.e., a larger proportion of mafic lithologies relative to depleted ambient mantle). As we observe, the amagmatic segment lavas are on average more enriched than the orthogonal supersegment lavas, thus reflecting the influence of a shortened melting column. However, Joseph Mayes Seamount and Narrowgate segment lavas are even more enriched than the amagmatic segment lavas, even though both of the former are orthogonal spreading segments. To address this inconsistency we need to constrain the zone of potential melt contribution or "effective segmentation."

[69] A magmatic segment's "effective segmentation" (grey ovals in Figure 15) is defined here as the zone of potential melt contribution, and is constrained by the across-axis, along-axis, and depth dimensions. All three dimensions are critical in determining the relative contribution of mafic versus host peridotite derived melts, thus the differences between the orthogonal and oblique supersegments provide a method for generating the gross compositional differences of their basalts. Here, however, we center our discussion on the across-axis and along-axis dimensions at the base of the melting region. Since the melting region narrows with decreasing depth (e.g., triangular melting zone), this provides a maximum estimate of the area of effective segmentation, which is critical to the contribution of mafic low-degree melts.

[70] We define the across-axis effective segmentation length as the perpendicular distance from the ridge axis to the point at which the upwelling mantle no longer passes through its solidus. Numerical modeling of the ridge thermal structure (L. Montesi, personal communication, 2007) at an ESR of 6.5 mm/a (half rate) suggests the mafic lithology solidus, approximated by the peridotite solidus [*Hirschmann*, 2000] minus ~200°C (from *Pertermann and Hirschmann* [2003] at 2 GPa), extends out to a distance much greater than the length of the magmatic segment. However, what is not considered in this numerical modeling is (1) how the increasing component of horizontal mantle flow influences melt focusing with distance from the ridge and (2) whether the slope of the base of the lithosphere (i.e., permeability layer and focusing mechanism) is steep enough to effectively focus melts from the distal "wings." Both these factors could limit the amount of melt focused toward the ridge and thus diminish the across-axis dimension of effective segmentation. As might be predicted, steeper isotherms result from a decrease in ESR, thus the across-axis dimension of effective segmentation is smaller on the oblique supersegment than the orthogonal.

[71] The along-axis effective segmentation length is the distance from one intersegment midpoint to the next, where the intersegment midpoint is the axial location with the thickest lithosphere between two magmatic segments. As discussed earlier, the axial lithospheric thickness is a direct function of the ESR, and therefore it could be estimated on the basis of conductive cooling. Where magmatic segments occur continuously (e.g., orthogonal supersegment), the along-axis dimension is equal to or only slightly larger than the measured length of the volcanic segment. Thus, with both the across-axis and along-axis dimensions constant, the effective segmentation does not change significantly. Where the intersegment midpoint spacing is asymmetric, as with the 16°E magmatic segment, the effective segmentation will be elongated in the direction of greater (midpoint) spacing (Figure 15). As a result of this asymmetric (along-axis) effective segmentation, the 16°E segment receives a greater proportion of enriched low-degree melts (from the neighboring amagmatic segment) than the rest of the orthogonal supersegment segments. Elevated K_2O and K/Ti in many basalts from this segment confirm this process (Figure 8).

[72] On the oblique supersegment, the along-axis effective segmentation length dramatically increases as the spacing between magmatic segment midpoints increases (Figure 15). This is likely more influential than similar scaling of the across-axis dimension, as mafic low-degree melts generated beneath (or near) the axis are more likely to be focused along a rheological barrier (i.e., crystallization front) [*Aharonov et al.*, 1995; *Kelemen and Aharonov*, 1998; *Korenaga and Kelemen*, 1998] toward a central point than melts generated in the distant wings of the melting region. Thus, along-axis melt focusing from beneath amagmatic segments to the magmatic segments likely accounts for the atypically large crustal thickness and enriched basalt chemistry of the latter. Numerical modeling by *Montesi et al.* [2006] shows 3-D focusing of melt trajectory pathways from beneath the amagmatic segments toward the neighboring Narrowgate segment and Joseph Mayes Seamount. Furthermore, their modeling documents quantitative differences in the total amount of partial melting and crustal thickness for each segment.

[73] Therefore, along-axis variability in lithospheric thickness and source mantle composition leads to the generation of deep, enriched low-F melts beneath the amagmatic segments. Because of the possible influence of increased mantle viscosity, which has been linked to the formation of pressure gradients and subsequent three-dimensional melt focusing [e.g., *Buck and Su*, 1989; *Magde and Sparks*, 1997; *Scott and Stevenson*, 1989; *Spiegelman and Reynolds*, 1999] and/or decreased vertical melt migration resulting from crystallization near the 1250°C isotherm, melt will likely migrate along the asthenosphere-lithosphere boundary [e.g., *Hall and Kincaid*, 2003; *Ito et al.*, 1999] toward segments with thinner lithosphere. This will produce aggregate melts beneath Joseph Mayes Seamount and Narrowgate segment more enriched than they would otherwise be without along-axis melt focusing. Last, the aggregate melts that remain beneath the amagmatic segments and erupt to the seafloor are on average more enriched then melts produced beneath the orthogonal supersegment, However, they also display a range from N-MORB to E-MORB. This reflects both the shortening of the melting column (e.g., low-F melts), the influence of melt-rock reaction during melt transport through the lithosphere, and the inefficiency of melt mixing beneath segments from which melts are focused away.

6. Conclusions

[74] 1. Detailed bathymetry and closely spaced sampling from 9 to 25°E on the SW Indian Ridge shows genetically significant correlations between ridge morphology, segmentation, lithology, and major element basalt chemistry. The along-axis basalt compositional variations require both a regional gradient in mantle source composition and the influence of variable lithospheric thickness and effective segmentation.

[75] 2. Fractionation-corrected H_2O contents between 0.18 and 0.60 wt % influence parental melt liquid lines of descent by suppressing crystallization of plagioclase and clinopyroxene to lower temperature (or lower MgO), thus allowing olivine to crystallize alone over a larger temperature range. Parental melts with elevated H_2O contents (E-MORBs) have decreased Fe_8 and increased Al_8 with lesser effects on Na_8, Si_8, and Ca_8. This influence accounts for a portion of the major element heterogeneity.

[76] 3. Orthogonal supersegment basalts lie squarely on the global array, but reflect lower extents of melting compared with average Indian Ocean, East Pacific Rise, and Mid-Atlantic Ridge basalt. This is consistent with the predicted effect of increased conductive cooling of the lithosphere from above, as a function of ultraslow spreading rates. The other tectonomagmatic provinces on the oblique supersegment lie off the array to lower Fe_8, which is partly explained by H_2O-influenced fractional crystallization.

[77] 4. Along-axis chemical variability of Fe_8, Na_8, K_8, H_8, and particularly K_8/Ti_8 cannot be explained by conventional passive upwelling models that rely on varying degrees of partial melting of a homogeneous peridotite source. Alternatively, we require a two-lithology mantle source containing a limited (<5%) proportion of mafic material within the ambient asthenosphere, likely originating from a previous melting event where the asthenosphere was metasomatized by pyroxenite melt.

[78] 5. We propose a model for MORB generation which illustrates the dramatic effects that spreading geometry can have on mantle thermal structure at spreading rates <20 mm/a. It provides insight into the mantle melting process and nature of the MORB source, so often obscured on faster spreading ridges where higher extents of melting more effectively sample the bulk mantle composition.

[79] Passive upwelling of a two-lithology mantle source triggers decompression partial melting of metasomatized mantle with mafic "pyroxenite" material much deeper (~100 km) than depleted peridotite (~55–60 km). As a result, the 3-D source volume for enriched pyroxenite melts is substantially larger than that for the anhydrous depleted peridotite, which influences the overall enrichment and compositional distribution of basalts. In response to changes in spreading geometry, conductive cooling is highly variable at the segment scale, especially along the oblique supersegment. The variation in lithospheric thickness between segments ultimately controls many of the important model parameters including, degree of melting, lithospheric topography (base), melt-mantle reaction, and effective segmentation. Relatively constant spreading geometry and rate along the orthogonal supersegment results in uniform effective segmentation and relatively constant lithospheric thickness and melt production. The 16°E segment diverges from this pattern of homogeneity as it is flanked to the west by an amagmatic segment, which causes the effective segmentation

of the 16°E magmatic segment to be elongated to the west. Along-axis focusing of melts containing a stronger pyroxenite signature serves to enrich the aggregate basalts, as seen by the increase in K_2O, H_2O, and K/Ti within these lavas.

[80] Farther to the west, drastically changing obliquity and ESR between segments, together with an alternating pattern of magmatic and amagmatic segmentation, generates variations in lithospheric thickness and effective segmentation that controls basalt compositional variability and distribution. On the basis of the fairly ubiquitous presence of E-MORB across all three tectonomagmatic provinces we surmise the proportion of pyroxenite within the oblique supersegment source is fairly constant despite the elevated K/Ti for the Narrowgate segment basalts. Instead, we attribute the enrichment spike at Narrowgate and the moderately elevated compositions at Joseph Mayes Seamount to the effects of mantle melting and melt transport processes. Increased effective segmentation along the oblique supersegment creates a significantly larger 3-D mantle volume from which partial melts are extracted and then focused along-axis according to the topography of the base of the lithosphere. Because of the flanking amagmatic segments and their thickened lithosphere, the majority of the melt focused along-axis toward either the Narrowgate segment or Joseph Mayes Seamount is generated by partial melting of pyroxenite and is highly enriched in incompatible elements. The addition of these enriched melts and resulting increase in melt volume is consistent with both the compositional distribution and the estimated crustal thickness at these segments. The more moderate enrichment in basalt compositions at Joseph Mayes Seamount relative to the Narrowgate segment can be attributed to its younger age and a less depleted mantle column with greater reactive capacity.

[81] 6. Finally, the mixed assemblage of N-MORB and E-MORB observed on the amagmatic segments, and the differences in the enrichment of the Joseph Mayes Seamount and Narrowgate basalts can be explained by a reactive transport melt-mantle reaction model where the mantle melting history and melt transport volumes are highly varied, which is generally not the case at faster effective spreading rates.

Acknowledgments

[82] The authors would like to thank Nancy Grindlay, John Madsen, and T. Dulaney for access to their full geophysical data set for the 16 to 25°E area. Sincere thanks are extended to the crew and scientific party on both the R/V *Knorr* 162, Legs VII to IX, in 2000–2001 and the R/V *Melville*, Vancouver 07 in 2003. J. S. would like to personally thank Peter Kelemen for numerous thought provoking discussions, along with Glenn Gaetani, Anton le Roex, Fred Frey, Jessica Warren, Laurent Montesi, and Mark Behn for their valuable discussions and contributions throughout this effort. The manuscript greatly benefited from official reviews by Rhea Workman and Jackie Dixon as well as informal comments from Jim Natland and Charlie Langmuir, all of whom are greatly thanked. The manuscript has also greatly improved following helpful advice and guidance from Vincent Salters (Editor). This work was originally funded in large part by NSF grants OCE-9907630 and OCE-0526905 and more recently by OPP-0425785.

References

Abelson, M., and A. Agnon (1997), Mechanics of oblique spreading and ridge segmentation, *Earth Planet. Sci. Lett.*, *148*(3–4), 405–421.

Aharonov, E., J. A. Whitehead, P. B. Kelemen, and M. Spiegelman (1995), Channeling instability of upwelling melt in the mantle, *J. Geophys. Res.*, *100*(B10), 20,433–20,450.

Asimow, P. D., and C. Langmuir (2003), The importance of water to oceanic mantle melting regimes, *Nature*, *421*, 815–820.

Asimow, P. D., J. E. Dixon, and C. H. Langmuir (2004), A hydrous melting and fractionation model for mid-ocean ridge basalts: Applications to the Mid-Atlantic Ridge near the Azores, *Geochem. Geophys. Geosyst.*, *5*, Q01E16, doi:10.1029/2003GC000568.

Baker, M. B., and E. M. Stolper (1994), Determining the composition of high-pressure mantle melts using diamond aggregates, *Geochim. Cosmochim. Acta*, *59*, 4489–4506.

Barry, J., M. D. Behn, and L. Montesi (2005), Melting and mantle flow beneath oblique ultraslow-spreading ridges, *Eos Trans. AGU*, *86*(52), Fall Meet. Suppl., Abstract T41E–1351.

Behn, M. D., C. P. Conrad, and P. G. Silver (2004), Detection of upper mantle flow associated with the African Superplume, *Earth Planet. Sci. Lett.*, *224*(3–4), 259–274.

Bender, J. F., F. N. Hodges, and A. E. Bence (1978), Petrogenesis of basalts from the Project FAMOUS Area: Experimental study from 0–15 kbars, *Earth Planet. Sci. Lett.*, *41*, 277–302.

Bown, J. W., and R. S. White (1994), Variation with spreading rate of oceanic crustal thickness and geochemistry, *Earth Planet. Sci. Lett.*, *121*, 435–439.

Braun, M. G., and P. B. Kelemen (2002), Dunite distribution in the Oman Ophiolite: Implications for melt flux through porous dunite conduits, *Geochem. Geophys. Geosyst.*, *3*(11), 8603, doi:10.1029/2001GC000289.

Buck, W. R., and W. Su (1989), Focused mantle upwelling below mid-ocean ridges due to feedback between viscosity and melting, *Geophys. Res. Lett.*, *16*, 641–644.

Cannat, M., C. Rommevaux-Jestin, and H. Fujimoto (2003), Melt supply variations to a magma-poor ultra-slow spreading ridge (Southwest Indian Ridge 61° to 69°E), *Geochem. Geophys. Geosyst.*, *4*(8), 9104, doi:10.1029/2002GC000480.

Cannat, M., D. Sauter, V. Mendel, E. Ruellan, K. Okino, J. Escartin, V. Combier, and M. Baala (2006), Modes of seafloor generation at a melt-poor ultraslow-spreading ridge, *Geology*, *34*(7), 605–608.

Cannat, M., D. Sauter, A. Bezos, C. M. Meyzen, E. Humler, and M. Le Rigoleur (2008), Spreading rate, spreading obliquity, and melt supply at the ultraslow spreading Southwest Indian Ridge, *Geochem. Geophys. Geosyst.*, *9*, Q04002, doi:10.1029/2007GC001676.

Christie, D. M., R. Werner, F. Hauff, K. Hoernle, and B. B. Hanan (2005), Morphological and geochemical variations along the eastern Galapagos Spreading Center, *Geochem. Geophys. Geosyst.*, *6*, Q01006, doi:10.1029/2004GC000714.

Cox, K. G., J. D. Bell, and R. J. Pankhurst (1979), *The Interpretation of Igneous Rocks*, Allen and Unwin, Boston, Mass.

Cushman, B., J. Sinton, G. Ito, and J. E. Dixon (2004), Glass compositions, plume-ridge interaction, and hydrous melting along the Galapagos Spreading Center, 90.5°W to 98°W, *Geochem. Geophys. Geosyst.*, *5*, Q08E17, doi:10.1029/2004GC000709.

Dick, H. J. B. (1977), Partial melting in the Josephine peridotite I, The effect on mineral composition and its consequence for geobarometry and geothermometry, *Am. J. Sci.*, *277*, 801–832.

Dick, H. J. B. (1989), Abyssal peridotites, very slow spreading ridges and ocean ridge magmatism, in *Magmatism in the Ocean Basins*, edited by A. D. Saunders and M. J. Norry, *Spec. Publ. Geol. Soc.*, *42*, 71–105.

Dick, H. J. B., and R. L. Fisher (1984), Mineralogic studies of the residues of mantle melting: Abyssal and alpine-type peridotites, in *Kimberlites II. The Mantle and Crust-Mantle Relationships*, edited by J. Kornprobst, pp. 295–308, Elsevier, Amsterdam.

Dick, H. J. B., R. L. Fisher, and W. B. Bryan (1984), Mineralogic variability of the uppermost mantle along mid-ocean ridges, *Earth Planet. Sci. Lett.*, *69*, 88–106.

Dick, H., J. Lin, and H. Schouten (2003), An ultraslow-spreading class of ocean ridge, *Nature*, *426*, 405–412.

Dixon, J. E., and E. Stolper (1995), An experimental study of water and carbon dioxide solubilities in mid-ocean ridge basaltic liquids, part II, Applications to degassing, *J. Petrol.*, *36*, 1633–1646.

Dixon, J. E., E. Stolper, and J. R. Holloway (1995), An experimental study of water and carbon dioxide solubilities in mid-ocean ridge basaltic liquids, part I, Calibrations and solubility models, *J. Petrol.*, *36*, 1607–1631.

Donnelly, K. E., S. L. Goldstein, C. Langmuir, and M. Spiegelman (2004), Origin of enriched ocean ridge basalts and implications for mantle dynamics, *Earth Planet. Sci. Lett.*, *226*(3–4), 347–366.

Dulaney, T. (2002), *Volcanic Morphology of the Ultraslow Spreading Southwest Indian Ridge (15°–35°E): Implications for Crustal Construction*, 203 pp., Univ. of N. C., Wilmington.

Elthon, D., R. D. Kent, and J. K. Meen (1995), Compositional variations of basaltic glasses from the Mid-Cayman Rise spreading center, *J. Geophys. Res.*, *100*(7), 12,497–12,512.

Engel, A. E. J., C. G. Engel, and R. G. Havens (1965), Chemical characteristics of oceanic basalts and the upper mantle, *Geol. Soc. Am. Bull.*, *76*, 719–734.

Engel, C. G., R. L. Fischer, and A. E. J. Engel (1965), Igneous rocks of the Indian Ocean Floor, *Science*, *150*, 605–610.

Fujiwara, T., J. Lin, T. Matsumoto, P. Kelemen, B. Tucholke, and J. Casey (2003), Crustal Evolution of the Mid-Atlantic Ridge near the Fifteen-Twenty Fracture Zone in the last 5 Ma, *Geochem. Geophys. Geosyst.*, *4*(3), 1024, doi:10.1029/2002GC000364.

Gaetani, G. A., and T. E. Grove (1998), The influence of water on melting of mantle peridotite, *Contrib. Mineral. Petrol.*, *131*, 323–346.

Galer, S. J. G., and R. K. O'Nions (1986), Magma genesis and the mapping of chemical and isotopic variations in the mantle, *Chem. Geol.*, *56*, 45–61.

Grindlay, N. R., J. A. Madsen, C. Rommevaux-Jestin, and J. Sclater (1998), A different pattern of ridge segmentation and mantle Bouguer gravity anomalies along the ultra-slow spreading Southwest Indian Ridge (15°30′E to 25°E), *Earth Planet. Sci. Lett.*, *161*, 243–253.

Grindlay, N., F. J. Madsen, T. Dulaney, and D. Smith (2000), Variations in axial relief and gravity anomalies at the Southwest Indian Ridge 15°–35°E, *Geophys. Res. Abstr.*, *2*, 47.

Grove, T. L., R. J. Kinzler, and W. B. Bryan (1992), Fractionation of Mid-Ocean Ridge Basalt (MORB), in *Mantle Flow and Melt Generation at Mid-Ocean Ridges*, *Geophys. Monogr. Ser.*, vol. 71, edited by J. P. Morgan, D. K. Blackman, and J. M. Sinton, pp. 281–310, AGU, Washington, D. C.

Hall, P. S., and C. Kincaid (2003), Melting, dehydration, and the dynamics of off-axis plume-ridge interaction, *Geochem. Geophys. Geosyst.*, *4*(9), 8510, doi:10.1029/2003GC000567.

Hanson, G. N. (1977), Geochemical evolution of the suboceanic mantle, *J. Geol. Soc. London*, *134*, 1–19.

Hart, S. R., and A. Zindler (1986), In search of a bulk-earth composition, *Chem. Geol.*, *57*, 247–267.

Herzberg, C. T. (2004), Partial crystallization of mid-ocean ridge basalts in the crust and mantle, *J. Petrol.*, *45*, 2389–2405.

Hirschmann, M. M. (2000), Mantle solidus: Experimental constraints and the effects of peridotite composition, *Geochem. Geophys. Geosyst.*, *1*(10), doi:10.1029/2000GC000070.

Hirschmann, M. M., and E. M. Stolper (1996), A possible role for garnet pyroxenite in the origin of the "garnet signature" in MORB, *Contrib. Mineral. Petrol.*, *124*(2), 185–208.

Hirschmann, M. M., T. Kogiso, M. B. Baker, and E. M. Stolper (2003), Alkalic magmas generated by partial melting of garnet pyroxenite, *Geology*, *31*, 481–484.

Ito, G., and J. J. Mahoney (2004a), Flow and melting of a heterogeneous mantle: 1. Method and importance to the geochemistry of ocean island and mid-ocean ridge basalts, *Earth Planet. Sci. Lett.*, *230*(1–2), 29–46.

Ito, G., and J. J. Mahoney (2004b), Flow and melting of a heterogeneous mantle: 2. Implications for a chemically nonlayered mantle, *Earth Planet. Sci. Lett.*, *230*(1–2), 47–63.

Ito, G., Y. Shen, G. Hirth, and C. J. Wolfe (1999), Mantle flow, melting, and dehydration of the Iceland mantle plume, *Earth Planet. Sci. Lett.*, *165*, 81–96.

Janney, P. E., A. P. le Roex, and R. W. Carlson (2005), Hafnium isotope and trace element constraints on the nature of mantle heterogeneity beneath the central Southwest Indian Ridge (13°E to 47°E), *J. Petrol.*, *46*(12), 2427–2464.

Jaques, A. L., and D. H. Green (1980), Anhydrous melting of peridotite at 0–15 Kb pressure and the genesis of tholeiitic basalts, *Contrib. Mineral. Petrol.*, *73*, 287–310.

Johnson, K. T. M., H. J. B. Dick, and N. Shimizu (1990), Melting in the oceanic upper mantle: An ion microprobe study of diopsides in abyssal peridotites, *J. Geophys. Res.*, *95*(B3), 2661–2678.

Jokat, W., and M. Schmidt-Aursch (2007), Geophysical characteristics of the ultraslow spreading Gakkel Ridge, Arctic Ocean, *Geophys. J. Int.*, *168*(3), 983–998.

Jokat, W., O. Ritzmann, M. C. Schmidt-Aursch, S. Drachev, S. Gauger, and J. E. Snow (2003), Geophysical evidence for reduced melt production on the Arctic ultraslow Gakkel mid-ocean ridge, *Nature*, *423*, 962–965.

Kelemen, P. B., and E. Aharonov (1998), Periodic formation of magma fractures and generation of layered gabbros in the lower

crust beneath oceanic spreading ridges, in *Faulting and Magmatism at Mid-Ocean Ridges*, *Geophys. Monogr. Ser.*, vol. 106, edited by W. Buck, P. T. Delaney, J. A. Karson, and Y. Lagabrielle, pp. 267–290, AGU, Washington, D. C.

Kelemen, P. B., and H. J. B. Dick (1995), Focused melt flow and localized deformation in the upper mantle: Juxtaposition of replacive dunite and ductile shear zones in the Josephine peridotite, SW Oregon, *J. Geophys. Res.*, *100*(B1), 423–438.

Kelemen, P., M. Braun, and G. Hirth (2000), Spatial distribution of melt conduits in the mantle beneath oceanic spreading ridges: Observations from the Ingalls and Oman ophiolites, *Geochem. Geophys. Geosyst.*, *1*(7), doi:10.1029/1999GC000012.

Kelemen, P., E. Kikawa, D. J. Miller, and the Shipboard Scientific Party (2007), Leg 209 summary: Processes in a 20-km-thick conductive boundary layer beneath the Mid-Atlantic Ridge, 14°–16°N, *Proc. Ocean Drill. Program Sci. Res.*, *209*, 1–33.

Kinzler, R. J. (1997), Melting of mantle peridotite at pressures approaching the spinel to garnet transition: application to mid-ocean ridge basalt petrogenesis, *J. Geophys. Res.*, *102*(B1), 853–874.

Kinzler, R. J., and T. Grove (1992), Primary magmas of mid-ocean ridge basalts 2. Applications, *J. Geophys. Res.*, *97*, 6907–6926.

Klein, E. M., and C. H. Langmuir (1987), Global correlations of ocean ridge basalt chemistry with axial depth and crustal thickness, *J. Geophys. Res.*, *92*, 8089–8115.

Kogiso, T., M. M. Hirschmann, and M. Pertermann (2004), High-pressure partial melting of mafic lithologies in the mantle, *J. Petrol.*, *45*, 2407–2422.

Korenaga, J., and P. B. Kelemen (1998), Melt migration through the oceanic lower crust: A constraint from melt percolation modeling with finite solid diffusion, *Earth Planet. Sci. Lett.*, *156*(1–2), 1–11.

Kushiro, I. (1964), The system diopside-forsterite-enstatite at 20 kilobars, *Carnegie Inst. Washington Year Book*, *63*, 101–108.

Kushiro, I. (1972), Effect of water on the composition of magmas formed at high pressures, *J. Petrol.*, *13*, 311–334.

Kushiro, I. (1975), Nature of silicate melt and its significance in magma genesis - Regularities in shift of liquidus boundaries involving olivine, pyroxene, and silica minerals, *Am. J. Sci.*, *275*, 411–431.

Langmuir, C. H., E. M. Klein, and T. Plank (1992), Petrological systematics of mid-ocean ridge basalts: Constraints on melt generation beneath ocean ridges, in *Mantle Flow and Melt Generation at Mid-Ocean Ridges*, *Geophys. Monogr. Ser.*, vol. 71, edited by J. P. Morgan, D. K. Blackman, and J. M. Sinton, pp. 183–280, AGU, Washington, D. C.

Langmuir, C., A. Bezos, S. Escrig, and S. Parman (2006), Hydrous mantle melting at ridges and back-arc basins, *Geochim. Cosmochim. Acta*, *70*, suppl. 1, A341.

le Roex, A. P., H. J. B. Dick, and R. L. Fisher (1989), Petrology and geochemistry of MORB from 25°E to 46°E along the Southwest Indian Ridge: evidence for contrasting styles of mantle enrichment, *J. Petrol.*, *30*, 947–986.

le Roex, A. P., H. J. B. Dick, and R. T. Watkins (1992), Petrogenesis of anomalous K-enriched MORB from the Southwest Indian Ridge: 11°53′E to 14°38′E, *Contrib. Mineral. Petrol.*, *110*, 253–268.

le Roux, P. J., A. le Roex, and J.-G. Schilling (2002a), MORB melting processes beneath the southern Mid-Atlantic Ridge (40–55°S): A role for mantle plume-derived pyroxenite, *Contrib. Mineral. Petrol.*, *144*, 206–229.

le Roux, P. J., A. le Roex, J.-G. Schilling, N. Shimizu, W. W. Perkins, and N. J. G. Pearce (2002b), Mantle heterogeneity beneath the southern Mid-Atlantic Ridge: Trace element evidence for contamination of ambient asthenospheric mantle, *Earth Planet. Sci. Lett.*, *203*, 479–498.

le Roux, P. J., A. P. le Roex, and J.-G. Schilling (2002c), Crystallization processes beneath the southern Mid-Atlantic Ridge (40–55°S), evidence for high-pressure initiation of crystallization, *Contrib. Mineral. Petrol.*, *142*, 582–602.

Lissenberg, C. J., and H. J. B. Dick (2008), Melt-rock reaction in the lower oceanic crust and its implications for the genesis of mid-ocean ridge basalt, *Earth Planet. Sci. Lett.*, in press.

Macdonald, G. A., and T. Katsura (1964), Chemical composition of Hawaiian lavas, *J. Petrol.*, *5*, 82–133.

Magde, L. S., and D. W. Sparks (1997), Three-dimensional mantle upwelling, melt generation, and melt migration beneath segment slow spreading ridges, *J. Geophys. Res.*, *102*(B9), 20,571–20,583.

McKenzie, D., and M. J. Bickle (1988), The volume and composition of melt generated by extension of the lithosphere, *J. Petrol.*, *29*, 625–679.

Menke, W. (2005), *Plate Velocity Calculator*, Lamont-Doherty Earth Obs., Palisades, N. Y. (Available at http://www.ldeo.columbia.edu/users/menke/plates.html)

Mével, C. (2003), Serpentinization of abyssal peridotites at mid-ocean ridges, *C. R. Geosci.*, *335*(10–11), 825–852.

Meyzen, C. M., M. J. Toplis, E. Humler, J. N. Ludden, and C. Mevel (2003), A discontinuity in mantle composition beneath the southwest Indian ridge, *Nature*, *421*, 731–733.

Meyzen, C. M., J. Blichert-Toft, J. N. Ludden, E. Humler, C. Mével, and F. Albarède (2007), Isotopic portrayal of the Earth's upper mantle flow field, *Nature*, *447*, 1069–1074.

Michael, P. J., and E. Bonatti (1985), Peridotite composition from the North Atlantic: regional and tectonic variations for partial melting, *Earth Planet. Sci. Lett.*, *73*, 91–104.

Michael, P. J., and R. Chase (1987), The influence of primary magma composition, H_2O and pressure on mid-ocean ridge basalt differentiation, *Contrib. Mineral. Petrol.*, *96*(2), 245–263.

Michael, P. J., and W. C. Cornell (1998), Influence of spreading rate and magma supply on crystallization and assimilation beneath mid-ocean ridges: Evidence from chlorine and major element chemistry of mid-ocean ridge basalts, *J. Geophys. Res.*, *103*(B8), 18,325–18,356.

Michael, P. J., et al. (2003), Magmatic and amagmatic seafloor generation at the ultraslow-spreading Gakkel Ridge, Arctic Ocean, *Nature*, *423*, 956–961.

Montesi, L. G. J., M. D. Behn, and J. Barry (2006), Mantle flow and melting at oblique segments of the Southwest Indian Ridge, *Geophys. Res. Abstr.*, *8*, 04319.

Niu, Y., and R. Batiza (1993), Chemical variation trends at fast and slow-spreading mid-ocean ridges, *J. Geophys. Res.*, *98*(B5), 7887–7903.

Niu, Y., and R. Batiza (1997), Trace element evidence from seamounts for recycled oceanic crust in the eastern Pacific mantle, *Earth Planet. Sci. Lett.*, *148*, 471–483.

O'Hara, M. J. (1985), Importance of the 'shape' of the melting regime during partial melting of the mantle, *Nature*, *314*, 58–62.

Okino, K., D. Curewitz, M. Asada, K. Tamaki, P. Vogt, and K. Crane (2002), Preliminary analysis of the Knipovich Ridge segmentation: Influence of focused magmatism and ridge obliquity on an ultraslow spreading system, *Earth Planet. Sci. Lett.*, *202*, 275–288.

Pertermann, M., and M. M. Hirschmann (2003), Partial melting experiments on a MORB-like pyroxenite between 2 and

3 GPa: Constraints on the presence of pyroxenite in basalt source regions from solidus location and melting rate, *J. Geophys. Res.*, *108*(B2), 2125, doi:10.1029/2000JB000118.

Plank, T., and C. H. Langmuir (1992), Effects of the melting regime on the composition of the oceanic crust, *J. Geophys. Res.*, *97*, 19,749–19,770.

Reid, I., and H. R. Jackson (1981), Oceanic spreading rate and crustal thickness, *Mar. Geophys. Res.*, *5*, 165–172.

Reiners, P. W. (1998), Reactive melt transport in the mantle and geochemical signatures of mantle-derived magmas, *J. Petrol.*, *39*(5), 1039–1061.

Salters, V. J. M., and H. J. B. Dick (2002), Mineralogy of the mid-ocean-ridge basalt source from neodymium isotopic composition of abyssal peridotites, *Nature*, *418*, 68–72.

Sauter, D., H. Carton, V. Mendel, M. Munschy, C. Rommevaux-Jestin, J.-J. Schott, and H. Whitechurch (2004), Ridge segmentation and the magnetic structure of the Southwest Indian Ridge (at 50°30′E, 55°30′E and 66°20′E): Implications for magmatic processes at ultraslow-spreading centers, *Geochem. Geophys. Geosyst.*, *5*, Q05K08, doi:10.1029/2003GC000581.

Schilling, J.-G., M. Zajac, R. Evans, T. Johnston, W. White, J. D. Devine, and R. Kingsley (1983), Petrologic and geochemical variations along the Mid-Atlantic Ridge from 29°N to 73°N, *Am. J. Sci.*, *283*, 510–586.

Scott, D. R., and D. J. Stevenson (1989), A self-consistent model of melting, magma migration, and buoyancy-driven circulation beneath mid-ocean ridges, *J. Geophys. Res.*, *94*, 2973–2988.

Sen, G. (1988), Petrogenesis of spinel lherzolite and pyroxenite suite xenoliths from the Koolau shield, Oahu, Hawaii: Implications for petrology of the post-eruptive lithosphere beneath Oahu, *Contrib. Mineral. Petrol.*, *100*(1), 61–91.

Shen, Y., and D. W. Forsyth (1995), Geochemical constraints on initial and final depths of melting beneath mid-ocean ridges, *J. Geophys. Res.*, *100*, 2211–2237.

Shimizu, N., J. M. Warren, and H. J. B. Dick (2006a), The effects of melt extraction and melt-rock reaction on abyssal peridotite geochemistry, *Geochim. Cosmochim. Acta*, *70*(18), suppl. 1, A586.

Shimizu, N., J. M. Warren, C. Sakaguchi, E. Nakamura, and H. J. B. Dick (2006b), Large local-scale isotopic heterogeneities for the MORB source mantle: A case study on the SWIR, *Geochim. Cosmochim. Acta*, *70*(18), suppl. 1, A585.

Sinton, J. M., S. M. Smaglik, J. J. Mahoney, and K. C. Macdonald (1991), Magmatic processes at superfast spreading mid-ocean ridges: Glass compositional variations along the East Pacific Rise 13°–23°S, *J. Geophys. Res.*, *96*, 6133–6155.

Small, C., and L. V. Danyushevsky (2003), Plate-kinematic explanation for mid-oceanic-ridge depth disontinuities, *Geology*, *31*(5), 399–402.

Snow, J. E., E. Hellebrand, A. Handt, F. Nauret, Y. Gao, S. Feig, Z. Jovanovic, and S. Gauger (2004), Lena Trough (Arctic Ocean): An oblique 'amagmatic' rift, *Eos Trans. AGU*, *85*(47), Fall Meet. Suppl., Abstract T11G–01.

Spiegelman, M., and J. R. Reynolds (1999), Combined dynamic and geochemical evidence for convergent melt flow beneath the East Pacific Rise, *Nature*, *402*, 282–285.

Standish, J. J. (2005), *The Influence of Ridge Geometry at the Ultraslow-Spreading Southwest Indian Ridge (9°–25°E): Basalt Composition Sensitivity to Variations in Source and Process*, 286 pp., Mass. Inst. of Technol. and Woods Hole Oceanogr. Inst., Woods Hole, Mass.

Standish, J. J., H. Dick, S. R. Hart, R. Workman, and A. le Roex (2004), Source enrichment versus degree of melting beneath the SWIR (9°–25°E), paper presented at Goldschmidt Conference, Geochem. Soc. of Am., Copenhagen.

Su, Y. J. (2002), *Mid-Ocean Ridge Basalt Trace Element Systematics: Constraints From Database Management, ICPMS Analyses, Global Data Compilation, and Petrologic Modeling*, 569 pp, Columbia Univ., New York.

Sun, S. S., and G. N. Hanson (1975), Origin of Ross Island basanitoids and limitations upon the heterogeneity of mantle sources for alkali basalts and nephelinites, *Contrib. Mineral. Petrol.*, *52*, 77–106.

Thompson, G., W. B. Bryan, and W. G. Melson (1980), Geological and geophysical investigation of the Mid-Cayman Rise Spreading Center: Geochemical variation and petrogenesis of basalt glasses, *J. Geol.*, *88*, 41–55.

Tormey, D. R., T. L. Grove, and W. B. Bryan (1987), Experimental petrology of normal MORB near the Kane Fracture Zone: 22°–25°N, mid-Atlantic ridge, *Contrib. Mineral. Petrol.*, *96*, 121–139.

Walter, M. J. (1998), Melting of garnet peridotite and the origin of komatiite and depleted lithosphere, *J. Petrol.*, *39*, 29–60.

Warren, J. M. (2007), *Geochemical and Rheological Constraints on the Dynamics of the Oceanic Upper Mantle*, 282 pp., Mass. Inst. of Technol. and Woods Hole Oceanogr. Inst., Woods Hole, Mass.

Warren, J. M., N. Shimizu, H. J. B. Dick, C. Sakaguchi, and E. Nakamura (2006), Peridotite heterogeneity along the ultra-slow spreading SWIR oblique supersegment, *Eos Trans. AGU*, *87*(52), Fall Meet. Suppl., Abstract V11G-06.

Weaver, B. L. (1991), The origin of ocean island basalt end-member compositions: Trace element and isotopic constraints, *Earth Planet. Sci. Lett.*, *104*, 381–397.

Weaver, J. S., and C. H. Langmuir (1990), Calculation of phase equilibrium in mineral-melt systems*Comput. Geosci.*, *16*, 1–19.

White, R. S., T. A. Minshull, M. J. Bickle, and C. J. Robinson (2001), Melt generation at very slow-spreading oceanic ridges: Constraints from geochemical and geophysical data, *J. Petrol.*, *42*(6), 1171–1196.

Yaxley, G. M., and D. H. Green (1998), Reactions between eclogite and peridotite: Mantle refertilization by subduction of oceanic crust, *Schweiz. Mineral. Petrogr. Mitt.*, *78*, 243–255.

Yoder, H. S., and C. E. Tilley (1962), Origin of basaltic magmas: Experimental study of natural and synthetic rock systems*J. Petrol.*, *3*, 342–532.

Zindler, A., H. Staudigel, and R. Batiza (1984), Isotope and trace element geochemistry of young Pacific seamounts: Implications for the scale of upper mantle heterogeneity, *Earth Planet. Sci. Lett.*, *70*, 175–195.